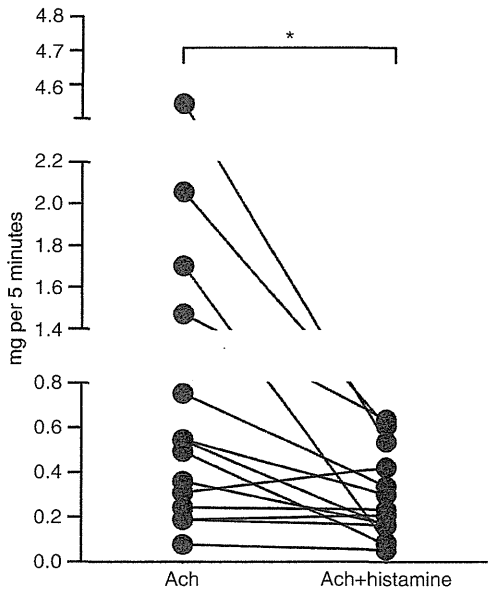

Figure 6. Histamine reduced axon reflex–mediated sweating volume in humans. The effect of simultaneous administration of histamine on quantitative sudomotor axon reflex test was assessed in the same individual ($n=13$). *$P<0.05$, paired *t*-test. Ach, acetylcholine.

sweating; similarly, H1R-KO mice showed diminished inhibition by histamine. As H1Rs are expressed in secretory sweat glands and nerve fibers, histamine might affect both tissues. These results indicate that H1R antagonists might have potential therapeutic effects in allergic patients with anhidrosis. Unexpected results were obtained from the administration of cimetidine and JN7777120; we found that these compounds decreased ACh-induced sweating but did not increase the low numbers of sweat pores positive for the iodine–starch reaction. These results suggest that an H2R or H4R antagonist might hold promise for treating hyperhidrosis. However, at present, we cannot explain the mechanisms of such phenomena; thus, further investigation is needed to clarify this issue.

We investigated the cross talk between the signaling pathways downstream of histamine and ACh, and found potential signal transducers that were differently activated by histamine or ACh. GSK3β is a Ser/Thr kinase with pleiotropic functions, including glycogen metabolism, regulation of the cell cycle, cell survival and differentiation, and inflammation (Doble and Woodgett, 2003; Jope and Johnson, 2004; Wang *et al*, 2011); it is phosphorylated in ACh-stimulated sweat glands. As GSK3β is also known to participate in the regulation of both cellular membrane transport and trafficking (Adachi *et al*, 2009; Rexhepaj *et al*, 2010), it is possible that GSK3β could be involved in sweat secretion (Supplementary Figure 4 online). When necessary, ACh causes the inactivation (phosphorylation) of GSK3β, stimulating sweat secretion. Histamine might inhibit ACh-induced sweat secretion by leading to the dephosphorylation (activation) of GSK3β. Previous reports about the function of GSK3β in glomerular filtration provide collateral evidence for this hypothesis. Mice with aberrantly activated GSK3β (gsk^{KI}) develop increased body temperature, food and water intake, glomerular filtration rate, urinary flow rate, urine osmolarity, urinary Na+ and K+, urea excretion, and proteinuria (Boini *et al*, 2008; Boini *et al*, 2009). Thus, it is easy to assume that activation of GSK3β might be involved in sweat secretion and glomerular filtration. This idea is supported by the dynamic images of sweat glands with two-photon microscopic analysis. To our knowledge, the real-time motion of sweat glands was previously unreported. The present study also revealed the inhibitory effects of histamine on GSK activation. As certain antihistamines affect glomerular filtration and renal function (Chansel *et al*, 1982; Abboud, 1983; Radke *et al*, 1985), histamine might affect the properties of secretory glands throughout the body.

AMP-activated protein kinase α1, a key regulator of intracellular fatty acid metabolism, is activated by increasing intracellular AMP levels (Liu *et al*, 2006); it is also inactivated by histamine administration. Unfortunately, although we could not confirm the function of AMP-activated protein kinase α1 in sweat glands, there is still the possibility that AMP-activated protein kinase α1 is involved in ACh-induced cAMP accumulation in sweat glands (Sato and Sato, 1983; 1987). Such attractive result should be confirmed elsewhere.

Dysfunctional sweating responses are not only problems for allergic dermatoses but also big problems for many types of diseases, including idiopathic anhidrosis or hyperhidrosis. Although these diseases strongly impair patients' quality-of-life, as well as activities of daily living, it should be said that there are no promising therapeutic methods for these diseases. We believe that this report may provide the basis of understanding the mechanisms involved and contribute to formulating therapeutic strategies for diseases involving sudomotor dysfunction.

MATERIALS AND METHODS

Animals

Ten- to twelve-week-old female C57BL/6J (C57BL/6) mice (10–12 weeks of age, weighing 20–30 g) were purchased from Clea (Osaka, Japan). H1R-KO (Hrh1 KO) mice were purchased from Oriental Bio Service (Kyoto, Japan). Mice were maintained in our pathogen-free animal facility. All animal care was in accordance with the institutional guidelines of Osaka University.

Preparation of reagents

ACh (pilocarpine hydrochloride; Junsei Chemical, Tokyo, Japan) and histamine (histamine diphosphate; Wako Pure Chemical Industries, Osaka, Japan) were dissolved in phosphate-buffered saline on the day of the experiment. Iodine (Sigma-Aldrich) was dissolved in ethanol (5% w/v) and starch (Wako Pure Chemical Industries) was diluted in mineral oil (nacalai tesque) (0.5% w/v).

In vivo sweat response

ACh-induced sweating was measured by both counting the spots in the starch–iodine reaction and measuring skin conductance to evaluate the number of active sweat glands and sweat volume, respectively.

The starch–iodine reaction was carried out using a slightly modified method from a previous report (Nejsum *et al*, 2002). Mice were anesthetized with intraperitoneal injection of a mixture of three drugs, 0.3 mg kg^{-1} domitor, 5 mg kg^{-1} vetorphale, and 4 mg kg^{-1} dormicum. Mouse hindpaws were painted with 3.5% iodine in

ethanol and 10% starch solution in mineral oil. Subsequently, subcutaneous injection with 20 μl phosphate-buffered saline (vehicle), 50 μg/20 μl ACh, and 120 μg/20 μl histamine was performed. The control group was the nontreated group. Each group consisted of 3–6 mice. Two minutes after injection, the treated hindpaws were photographed, and black spots caused by the amylase reaction (i.e., iodine and starch response) were counted.

Optical coherence tomography

Because there is a large refractive index difference on the wall of the spiral lumen between the sweat and keratinous epidermal tissues, the eccrine sweat ducts in the stratum corneum of the epidermis are clearly recognized by a spiral lumen with a high reflective light intensity. The dynamic OCT images of Ach-induced sweating in the *x–z* plane were obtained from B-mode OCT. The administration methods for vehicle, ACh, and histamine were the same as in the starch–iodine reaction test.

Two-photon excitation fluorescence microscopy

Intravital multiphoton imaging of sweat glands in the skin was performed using previously described protocols (Ishii *et al*, 2009) with modifications. Mice were anesthetized with isoflurane (Escain; 2.0% vaporized in 100% oxygen). Skin was observed with an inverted multiphoton microscope (A1R-MP; Nikon, Tokyo, Japan) driven by a Ti:Sapphire laser (Chameleon Vision II; Coherent, Santa Clara, CA) tuned to 800 nm and an inverted microscope equipped with multi-immersion objectives (CFI-Plan-Fluor, ×20/N.A. 0.75; Nikon). Sweat glands were visualized by anti-M3 antibody staining, and blood vessels were visualized using Texas Red-labeled 70-kDa dextran. To detect second harmonic-generated (ch1), FITC (ch2), Red (ch3), and Far Red (ch4) emission signals, 492 nm short pass, 500/50 nm, 562/25 nm, and 601/56 nm bandpass filters were used, respectively. Raw imaging data were processed with Volocity three-dimensional image analysis software (PerkinElmer, Waltham, MA). Sweat glands, microvessels, and nuclei were stained with FITC-conjugated anti-gross cystic disease fluid protein antibody or anti-aquaporin5 antibody, Texas Red-conjugated 70-kDa dextran, and Hoechst 33342, respectively.

Phosphorylation antibody array

Skin samples of mice hindpaws were obtained immediately after subcutaneous injection of Ach with or without histamine, or vehicle. Samples were lysed in buffer containing phosphatase inhibitor. The Phospho-Kinase-Array kit (proteome profiler antibody array; R&D Systems, Minneapolis, MN) was used according to the manufacturer's instructions.

Histamine antagonism

For histamine antagonism, 15 minutes before subcutaneous injection of ACh or histamine, mice were injected intraperitoneally with pyrilamine (700 μg per body), fexofenadine hydrochloride (600 μg per body), and cimetidine (400 μg per body).

Quantitative sudomotor axon reflex test

This study was approved by the Institutional Review Board of Osaka University hospital (ID: UMIN000009247). Healthy volunteers were enrolled in this study after obtaining a written informed consent and providing written and oral information to the study physicians. This study was performed in adherence with the guidelines of the Declaration of Helsinki.

An examination was performed on the basis of the method established by Lee *et al* (2009) (Kijima *et al*, 2012). Briefly, the subjects were asked to remain quiet for 60 minutes before undergoing QSART in a hospital outpatient clinic at constant temperature (20 °C) and humidity (60%). The sweat volume–measuring capsule and digital analyzer of measured sweat volume (SKINOS SKD-2000, Nagano, Japan) were used in QSART. ACh (100 mg ml^{-1}) with or without histamine (0.1 ~ 1% w/v) was iontophoretically applied to the skin from the outer compartment, whereas the glands of the skin in the central compartment of the capsule were activated indirectly via an axon reflex sweating. The axon reflex sweating volume was measured during the 5 minutes of iontophoresis. Data for DIR sweating were obtained over the subsequent 5 minutes.

Histological analysis

Paraffin-embedded samples of hindpaw skin were cut to 4-μm thick sections. The antibodies used were rabbit anti-M3 (Abcam, Cambridge, UK), goat anti-H1R, -H2R, and -H4R (all from Santa Cruz Biotechnology, Santa Cruz, CA), anti-protein gene product-9.5 (Chemicon; AB1761), and anti-SMA (Santa Cruz Biotechnology) antibodies. Secondary antibodies used were anti-rabbit and anti-goat conjugated to Alexa Fluor 488 (Invitrogen, Carlsbad, CA), and anti-rabbit and mouse antibodies conjugated to Alexa Fluor 555 (Invitrogen). Images of immunolabeled sections were captured with a BZ-8000 microscope (Keyence, Osaka, Japan).

Western blot analysis

Skin samples were crushed in liquid nitrogen and solubilized at 4 °C in lysis buffer (0.5% sodium deoxycholate, 1% Nonidet P40, 0.1% sodium dodecyl sulfate, 100 μg ml^{-1} phenylmethylsulphonyl fluoride, 1 mM sodium orthovanadate, and protease inhibitor cocktail). The protein extracts (20 μg each) were analyzed with an anti-phospho-GSK3α/β antibody (no. 9331, Cell Signaling Technology, Danvers, MA). An anti-GSK3α/β antibody (no. 5676; Cell Signaling Technology) was used as a control. Protein bands were detected using the ECL Plus kit (GE Healthcare, Buckinghamshire, UK). GSK3β was detected as two bands around 45 kDa. The intensity of the bands was quantified by using NIH image J software.

Statistic analysis

Prism5 software (GraphPad Software, La Jolla, CA) was used for statistical analysis. Statistical significance was examined by unpaired *t*-test or Bonferroni's multiple comparison test. Graph bars represent the mean ± SD. $*P<0.05$, $**P<0.01$, $***P<0.001$, and $****P<0.0001$.

CONFLICT OF INTEREST

The authors state no conflict of interest.

ACKNOWLEDGMENTS

We thank Ms Kumiko Mitsuyama, Ms Ryoko Sugiyama, Ms Maiko Sugiura, and Ms Kaori Kuroda for secretarial work, and Mr Kenju Nishida, Mrs Yoshiko Nobuyoshi, and Ms Sayaka Matsumura for research assistance. This study was supported by a research grant from the Ministry of Health, Labour and Welfare, Japan, Ministry of Education, Culture, Sports, Science and Technology, Japan, and a research grant from The Cosmetology Research Foundation.

SUPPLEMENTARY MATERIAL

Supplementary material is linked to the online version of the paper at http://www.nature.com/jid

REFERENCES

Abboud HE (1983) Catabolism of histamine in the isolated glomeruli and tubules of the rat kidney. *Kidney Int* 24:534–41

Adachi A, Kano F, Saido TC *et al.* (2009) Visual screening and analysis for kinase-regulated membrane trafficking pathways that are involved in extensive beta-amyloid secretion. *Genes Cells* 14:355–69

Akdis CA, Akdis M, Bieber T *et al.* (2006) Diagnosis and treatment of atopic dermatitis in children and adults: European Academy of Allergology and Clinical Immunology/American Academy of Allergy, Asthma and Immunology/PRACTALL Consensus Report. *Allergy* 61:969–87

Boini KM, Amann K, Kempe D *et al.* (2009) Proteinuria in mice expressing PKB/SGK-resistant GSK3. *Am J Physiol Renal Physiol* 296: F153–9

Boini KM, Bhandaru M, Mack A *et al.* (2008) Steroid hormone release as well as renal water and electrolyte excretion of mice expressing PKB/SGK-resistant GSK3. *Pflugers Arch* 456:1207–16

Chansel D, Oudinet JP, Nivez MP *et al.* (1982) Histamine H2 receptors in rat renal glomeruli. *Biochem Pharmacol* 31:367–75

Doble BW, Woodgett JR (2003) GSK-3: tricks of the trade for a multi-tasking kinase. *J Cell Sci* 116:1175–86

Du Buske LM (1996) Clinical comparison of histamine H1-receptor antagonist drugs. *J Allergy Clin Immunol* 98:S307–18

Eishi K, Lee JB, Bae SJ *et al.* (2002) Impaired sweating function in adult atopic dermatitis: results of the quantitative sudomotor axon reflex test. *Br J Dermatol* 147:683–8

Ertam I, Biyikli SE, Yazkan FA *et al.* (2007) The frequency of nasal carriage in chronic urticaria patients. *J Eur Acad Dermatol Venereol* 21:777–80

Fujikura T, Shimosawa T, Yakuo I (2001) Regulatory effect of histamine H1 receptor antagonist on the expression of messenger RNA encoding CC chemokines in the human nasal mucosa. *J Allergy Clin Immunol* 107: 123–8

Gengo FM, Manning C (1990) A review of the effects of antihistamines on mental processes related to automobile driving. *J Allergy Clin Immunol* 86:1034–9

Giustizieri ML, Albanesi C, Fluhr J *et al.* (2004) H1 histamine receptor mediates inflammatory responses in human keratinocytes. *J Allergy Clin Immunol* 114:1176–82

Imayama S, Shimozono Y, Hoashi M *et al.* (1994) Reduced secretion of IgA to skin surface of patients with atopic dermatitis. *J Allergy Clin Immunol* 94:195–200

Ishii M, Egen JG, Klauschen F *et al.* (2009) Sphingosine-1-phosphate mobilizes osteoclast precursors and regulates bone homeostasis. *Nature* 458:524–8

Itakura E, Urabe K, Yasumoto S *et al.* (2000) Cholinergic urticaria associated with acquired generalized hypohidrosis: report of a case and review of the literature. *Br J Dermatol* 143:1064–6

Jope RS, Johnson GV (2004) The glamour and gloom of glycogen synthase kinase-3. *Trends Biochem Sci* 29:95–102

Kijima A, Murota H, Matsui S *et al.* (2012) Abnormal axon reflex-mediated sweating correlates with high state of anxiety in atopic dermatitis. *Allergol Int* 61:469–73

Kitaba S, Matsui S, Iimuro E *et al.* (2011) Four cases of atopic dermatitis complicated by Sjogren's syndrome: link between dry skin and autoimmune anhidrosis. *Allergol Int* 60:387–91

Kobayashi H, Aiba S, Yamagishi T *et al.* (2002) Cholinergic urticaria, a new pathogenic concept: hypohidrosis due to interference with the delivery of sweat to the skin surface. *Dermatology* 204:173–8

Lee JB, Bae JS, Matsumoto T *et al.* (2009) Tropical Malaysians and temperate Koreans exhibit significant differences in sweating sensitivity in response to iontophoretically administered acetylcholine. *Int J Biometeorol* 53 149–57

Lin JS, Sakai K, Jouvet M (1988) Evidence for histaminergic arousal mechanisms in the hypothalamus of cat. *Neuropharmacology* 27:111–22

Liu Y, Wan Q, Guan Q *et al.* (2006) High-fat diet feeding impairs both the expression and activity of AMPKa in rats' skeletal muscle. *Biochem Biophys Res Commun* 339:701–7

Masaki T, Chiba S, Yasuda T *et al.* (2004) Involvement of hypothalamic histamine H1 receptor in the regulation of feeding rhythm and obesity. *Diabetes* 53:2250–60

Meltzer EO (1990) Performance effects of antihistamines. *J Allergy Clin Immunol* 86:613–9

Metz M, Doyle E, Bindslev-Jensen C *et al.* (2011) Effects of antihistamines on innate immune responses to severe bacterial infection in mice. *Int Arch Allergy Immunol* 155:355–60

Murota H, Katayama I (2011) Assessment of antihistamines in the treatment of skin allergies. *Curr Opin Allergy Clin Immunol* 11:428–37

Nejsum LN, Kwon TH, Jensen UB *et al.* (2002) Functional requirement of aquaporin-5 in plasma membranes of sweat glands. *Proc Natl Acad Sci USA* 99:511–6

Ohkuma S, Poole B (1978) Fluorescence probe measurement of the intralysosomal pH in living cells and the perturbation of pH by various agents. *Proc Natl Acad Sci USA* 75:3327–31

Ohmi M, Tanigawa M, Yamada A *et al.* (2009) Dynamic analysis of internal and external mental sweating by optical coherence tomography. *J Biomed Opt* 14:014026

Papa CM, Kligman AM (1966) Mechanisms of eccrine anidrosis.I. High level blockade. *J Invest Dermatol* 47:1–9

Radke KJ, Selkurt EE, Willis LR (1985) The role of histamine H1 and H2 receptors in the canine kidney. *Ren Physiol* 8:100–11

Rexhepaj R, Dermaku-Sopjani M, Gehring EM *et al.* (2010) Stimulation of electrogenic glucose transport by glycogen synthase kinase 3. *Cell Physiol Biochem* 26:641–6

Rieg S, Steffen H, Seeber S *et al.* (2005) Deficiency of dermcidin-derived antimicrobial peptides in sweat of patients with atopic dermatitis correlates with an impaired innate defense of human skin in vivo. *J Immunol* 174:8003–10

Sato K, Sato F (1983) Cholinergic potentiation of isoproterenol-induced cAMP level in sweat gland. *Am J Physiol* 245:C189–95

Sato K, Sato F (1987) Effect of VIP on sweat secretion and cAMP accumulation in isolated simian eccrine glands. *Am J Physiol* 253:R935–41

Schittek B, Paulmann M, Senyurek I *et al.* (2008) The role of antimicrobial peptides in human skin and in skin infectious diseases. *Infect Disord Drug Targets* 8:135–43

Schmid-Wendtner MH, Korting HC (2006) The pH of the skin surface and its impact on the barrier function. *Skin Pharmacol Physiol* 19:296–302

Shiohara T, Doi T, Hayakawa J (2011) Defective sweating responses in atopic dermatitis. *Curr Probl Dermatol* 41:68–79

Simons FE, Simons KJ (2011) Histamine and H1-antihistamines: celebrating a century of progress. *J Allergy Clin Immunol* 128:e4

Sugawara T, Kikuchi K, Tagami H *et al.* (2012) Decreased lactate and potassium levels in natural moisturizing factor from the stratum corneum of mild atopic dermatitis patients are involved with the reduced hydration state. *J Dermatol Sci* 66:154–9

Sulzberger MB, Herrmann F, Zak FG (1947) Studies of sweating; preliminary report with particular emphasis of a sweat retention syndrome. *J Invest Dermatol* 9:221–42

Vanbervliet B, Akdis M, Vocanson M *et al.* (2011) Histamine receptor H1 signaling on dendritic cells plays a key role in the IFN-gamma/IL-17 balance in T cell-mediated skin inflammation. *J Allergy Clin Immunol* 127:e1–10

Vilches JJ, Navarro X, Verdu E (1995) Functional sudomotor responses to cholinergic agonists and antagonists in the mouse. *J Auton Nerv Syst* 55: 105–11

Wang H, Brown J, Martin M (2011) Glycogen synthase kinase 3: a point of convergence for the host inflammatory response. *Cytokine* 53:130–40

DOI: 10.1111/exd.12284
www.wileyonlinelibrary.com/journal/EXD

Letter to the Editor

Topical cholesterol treatment ameliorates hapten-evoked cutaneous hypersensitivity by sustaining expression of 11β-HSD1 in epidermis

Hiroyuki Murota[1], Saori Itoi[1], Mika Terao[1], Saki Matsui[1], Hiromi Kawai[2], Yasunari Satou[2], Kazuma Suda[2] and Ichiro Katayama[1]

[1]Department of Dermatology, Osaka University, Osaka, Japan; [2]Rohto Pharmaceutical Co., Osaka, Japan
Correspondence: Hiroyuki Murota, 2-2 Yamadaoka, Suita, Osaka 5650871, Japan, Tel.: +81668793031, Fax: +81668793039, e-mail: h-murota@derma.med.osaka-u.ac.jp

Abstract: Changes in the stratum corneum extracellular matrix impair epidermal barrier function and may cause dermatoses. The aim of this study was to examine the effect of exogenous cholesterol application on skin barrier function and cutaneous inflammation. Skin barrier-disrupted or hapten-stimulated mice were treated with topical cholesterol. The effect of topical cholesterol application on an oxazolone (OXA)-induced hypersensitivity reaction was evaluated. Topical application of cholesterol efficiently decreased transepidermal water loss in areas of barrier-disrupted skin and ameliorated OXA-induced cutaneous hypersensitivity. These favourable effects may have resulted from sustained expression of 11β-hydroxysteroid dehydrogenase type 1 (11β-HSD1) in the cholesterol-treated skin. As 11β-HSD1 is known to produce active cortisol, topical cholesterol may attenuate contact hypersensitivity by normalizing secretion of hormonally active cortisol from the skin.

Key words: 11β-hydroxysteroid dehydrogenase type 1 – cholesterol – contact hypersensitivity – skin barrier – stratum corneum

Accepted for publication 11 November 2013

Background

An altered epidermal barrier function may result in the induction of various dermatoses (1). The stratum corneum contains various lipids, such as ceramides, cholesterol and free fatty acids, that act as biological barriers against pathogens and various sensitizers (1,2). Previous studies have shown that alteration of the lipid profile, including reduction in the total amount of ceramides and ceramidase activity, is responsible for functional abnormalities in skin with eczema, such as atopic dermatitis (AD) and contact dermatitis (3–5). Moreover, it has been reported that use of a physiological lipid mixture improves skin barrier function more effectively than use of topical ceramides (6,7). These results suggest that both ceramides and cholesterol are required for maintenance and recovery of skin's barrier function. Studies are needed that explore the outcome and impact of cholesterol that is solely applied topically.

Questions addressed

How does topical application of cholesterol impact the skin barrier function or hapten-evoked allergic reaction?

Experimental design

To investigate effects on barrier-disrupted skin, cholesterol was dissolved in chloroform (5% w/w; 0.17 M). Chloroform was used in the vehicle-treated group. We referred to the previous methodology to prepare the skin barrier-disrupted model using BALB/c mice (8). Cholesterol or vehicle was applied immediately after barrier disruption. Transepidermal water loss (TEWL) was measured over time, after application of cholesterol or vehicle.

Procedures for preparing cholesterol (5% w/w) or reference ointment are in the Data S1. Mice were treated with these ointments once a day for 1 week. TEWL was measured over time, after application of ointments.

Topical cholesterol was prepared by dissolving cholesterol in 0.5% (~0.01 M) and 2.5% (~0.05 M) w/w acetone to evaluate the impact of topical cholesterol on the oxazolone (OXA)-induced contact hypersensitivity reaction (CHR). Acetone was used as the vehicle control. Cholesterol or vehicle was applied to challenged ears 15 min after application of OXA. Methodology for induction of CHR is detailed in the Data S1.

Quantitative, real-time polymerase chain reaction (RT-PCR) and immunohistochemical staining were performed as previously described (9,10).

Statistical significance was examined using an unpaired *t*-test (Fig. 1a,b) or a one-way ANOVA and Bonferroni's multiple comparison test (Fig. 2a–c). Values of $P < 0.05$ were considered statistically significant.

Results

In our investigation of the ability of topical cholesterol to improve an impaired skin barrier, the cholesterol-treated group maintained low measurements of TEWL throughout the experiment. In contrast, TEWL in the vehicle-treated group increased immediately after the disruption of stratum corneum. TEWL measurements began to decrease 7 h after barrier disruption (Fig. 1a). The TEWL results led us to hypothesize that treatment with moisturizer containing cholesterol will generate an additive ameliorating effect on damaged skin barrier. Thus, we prepared cholesterol ointment and determined the safety of this ointment. We applied cholesterol or reference ointment on the skin once a day for 1 week. Unexpectedly, in the reference ointment-treated group, TEWL measurements began to increase 3 days after the initiation

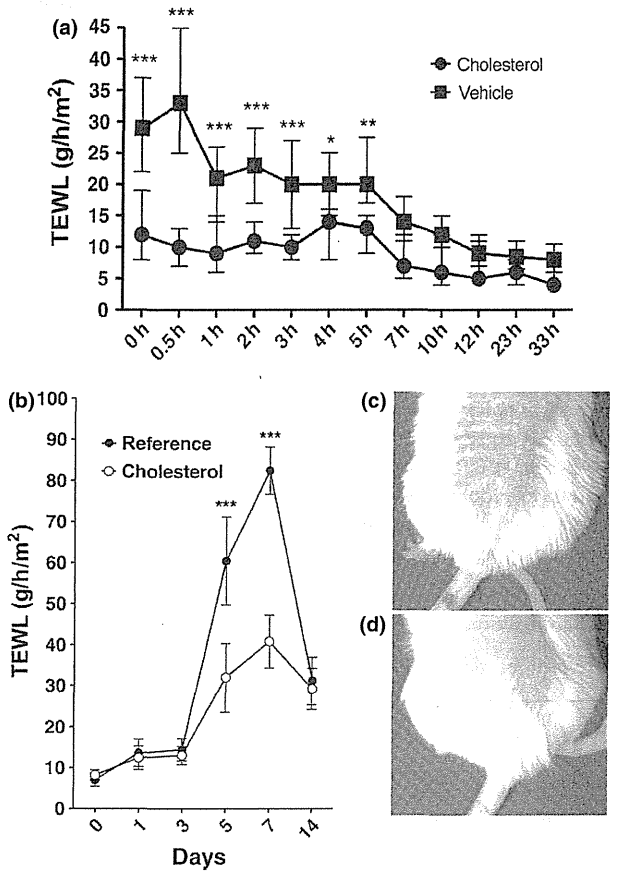

Figure 1. Cholesterol reduces contact dermatitis. (a) TEWL measurements to evaluate the effect of topical cholesterol (dissolved in chloroform) application on barrier-disrupted skin over time. Cholesterol: $n = 6$. Vehicle (chloroform): $n = 6$. (b) TEWL was measured after topical application of cholesterol ointment each day up to day 7 and then on day 14. Cholesterol ointment: $n = 5$. Reference ointment: $n = 5$. (a, b) Asterisks indicated $^{*}P < 0.05$, $^{**}P < 0.01$ and $^{***}P < 0.001$ (unpaired *t*-test). All symbols and error bars represent the mean ± SD. (c, d) Photographs of skin after 7 days of treatment with (c) reference ointment and with (d) cholesterol ointment.

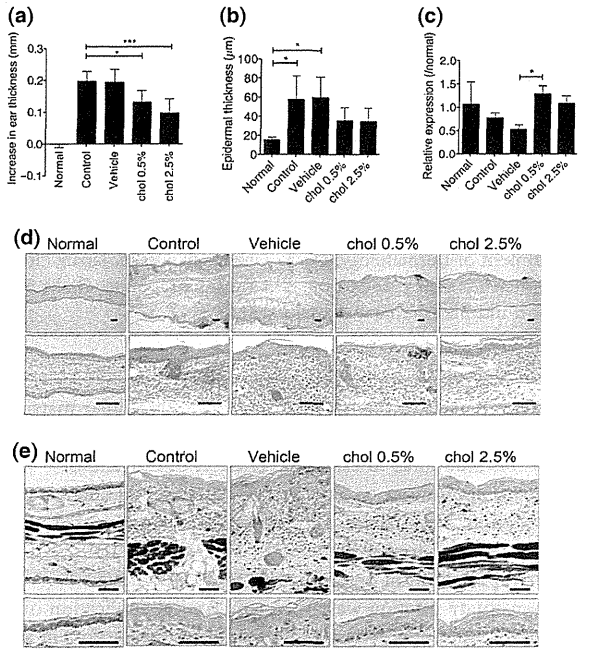

Figure 2. The effect of topical cholesterol on OXA-induced contact hypersensitivity reaction. (a) Ear thickness measured 24 h after OXA challenge. (b) Epidermal thickness measured 24 h after OXA challenge. Normal ($n = 3$): without any treatment. Control ($n = 3$): challenged with OXA without any treatment. Vehicle ($n = 3$): challenged with OXA and treated with vehicle ointment. Chol 0.5% or 2.5% ($n = 3$ each): challenged with OXA and treated with cholesterol ointment at the indicated concentration. (c) Real-time PCR analysis was performed to evaluate the expression of 11β-HSD1 in OXA-challenged skin with or without cholesterol application. (a–c) Asterisks indicated $^{*}P < 0.05$ and $^{***}P < 0.0011$ (Bonferroni's multiple comparison test). Graph bars represent the mean ± SD. (d) Histological analysis of treated ears. Top row: low magnification. Bottom row: high magnification. Bar = 100 µm. (e) Immunohistochemical staining for 11β-HSD1 in OXA-challenged skin ($n = 3$ each). Top row: low magnification. Bottom row: high magnification. Bar = 100 µm.

of treatment and continued to increase until discontinuation of the treatment (Fig. 1b). The skin area treated with reference ointment for 7 days exhibited induration and erythema with scales (Fig. 1c). On the other hand, TEWL measurements in the cholesterol ointment-treated group were significantly lower than those of the reference ointment-treated group (Fig. 1b). The cholesterol ointment treatment group did not develop any observable skin symptoms throughout the duration of the experiment (Fig. 1d). These results indicate that topical cholesterol application may reduce the severity of contact dermatitis. To confirm this, we evaluated the effect of cholesterol solubilized with acetone on an OXA-induced CHR. Topical cholesterol treatment ameliorated ear thickness in this experiment (Fig. 2a). Both cholesterol concentration of 0.5% and 2.5% showed comparable attenuating effects (Fig. 2a). Histological evaluation of lesional skin revealed that topical cholesterol application reduced oedema and the inflammatory infiltrate (Fig. 2b,d). As topical application of cholesterol reduced epidermal thickness (Fig. 2b), we examined expression of 11β-HSD1, a regulator of keratinocyte proliferation. The expression of 11β-HSD1 decreased in vehicle-treated inflamed skin compared to normal or control skin. However, 11β-HSD1 normalized in skin pretreated with topical cholesterol, compared to vehicle-treated inflamed skin (Fig. 2c). Expression of 11β-HSD1 in cholesterol-treated skin was confirmed with immunostaining (Fig. 2e). The consistent nature of the intensity of positive-staining muscle fibres in each tissue type analysed suggests that the expression of 11β-HSD1 in the epidermis of the cholesterol-treated groups normalized, compared to that of normal or vehicle-treated groups (Fig. 2e).

Conclusions

Our study demonstrated that topical application of cholesterol to barrier-disrupted skin maintained TEWL at a low level and ameliorated CHR. Interestingly, expression of 11β-HSD1, which was decreased in OXA-treated epidermis, was normalized in cholesterol-treated skin.

Previous studies suggest that cholesterol does not just exist in the extracellular matrix of the stratum corneum, but might be required to achieve proper levels of ceramide and function of the stratum corneum (2,11,12). Furthermore, it has been reported that exogenous cholesterol provides keratinocytes with photoprotection against UVA (13). Our results also indicated that topical cholesterol had a favourable effect on damaged skin. Therefore, we

suggest that cholesterol, in addition to ceramides, should be applied to barrier-disrupted skin (6,7).

Our interesting finding was that cholesterol ointment decreased OXA-induced CHR. As far as we know, there has been no report which describes such a favourable effect for topical application of cholesterol on a CHR. Real-time PCR and histological analyses revealed the possible involvement of 11β-HSD1, which converts cortisone to active cortisol, as a mechanism of cholesterol-induced attenuation of CHR. As cortisol has potent anti-inflammatory effects, the expression level of 11β-HSD1 may influence immune responses (14). It has also been reported that 11β-HSD1 regulates keratinocyte proliferation, but not differentiation (9,10). This knowledge taken together suggests that cholesterol might attenuate the contact hypersensitivity reaction partly via sustained expression of 11β-HSD1 in our mouse models. Thus, a cholesterol-induced endogenous steroid might be an alternative therapy to the use of exogenous steroids. Although further studies are required to reveal the more precise mechanism, it might be speculated that exogenous cholesterol application can improve and prevent CHR.

Acknowledgements

The authors thank Ms. Kumiko Mitsuyama, Ms. Ryoko Sugiyama and Ms. Maiko Sugiura for secretarial work. We would also like to thank Mr. Kenju Nishida and Ms. Eriko Nobuyoshi for assistance with research.

Funding source

This study was supported in part by a research grant from the Ministry of Health, Labour and Welfare, Japan.

Conflict of interests

The authors have no conflict of interests to declare. This study was performed as joint research between industry and our university.

References

1 Angelova-Fischer I, Mannheimer A C, Hinder A *et al.* Exp Dermatol 2011: **20**: 351–356.
2 Elias P M. J Invest Dermatol 2012: **132**: 2131–2133.
3 Imokawa G, Abe A, Jin K *et al.* J Invest Dermatol 1991: **96**: 523–526.
4 Janssens M, van Smeden J, Gooris G S *et al.* J Invest Dermatol 2011: **131**: 2136–2138.
5 Proksch E, Brandner J M, Jensen J M. Exp Dermatol 2008: **17**: 1063–1072.
6 Elias P M, Wakefield J S. Clin Rev Allergy Immunol 2011: **41**: 282–295.
7 Elias P M. Clin Med Dermatol 2009: **2**: 1–3.
8 Tominaga M, Ozawa S, Tengara S *et al.* J Dermatol Sci 2007: **48**: 103–111.
9 Terao M, Murota H, Kimura A *et al.* PLoS ONE 2011: **6**: e25039.
10 Terao M, Itoi S, Murota H *et al.* Exp Dermatol 2013: **22**: 98–101.
11 Iwai I, Han H, den Hollander L *et al.* J Invest Dermatol 2012: **132**: 2215–2225.
12 Feingold K R, Jiang Y J. Dermatoendocrinol 2011: **3**: 113–118.
13 Bayer M, Proksch P, Felsner I *et al.* Exp Dermatol 2011: **20**: 955–958.
14 Coutinho A E, Gray M, Brownstein D G *et al.* Endocrinology 2012: **153**: 234–240.

Supporting Information

Additional Supporting Information may be found in the online version of this article:

Data S1. Supplemental information of experimental design.

DOI: 10.1111/exd.12291
www.wileyonlinelibrary.com/journal/EXD

Letter to the Editor

Regional difference in sebum production by androgen susceptibility in human facial skin

Young Joon Seo[1], Zheng Jun Li[1], Dae Kyoung Choi[1], Kyung Cheol Sohn[1], Hyeong Rae Kim[1], Young Lee[1], Chang Deok Kim[1], Young Ho Lee[2], Ge Shi[3], Jeung Hoon Lee[1] and Myung Im[1]

[1]Department of Dermatology, College of Medicine, Chungnam National University, Daejeon, Korea; [2]Department of Anatomy, College of Medicine, Chungnam National University, Daejeon, Korea; [3]Department of Dermatology, The Affiliated Hospital of Guangdong Medical College, Zhanjiang, China

Correspondence: Myung Im, MD, PhD, Department of Dermatology, Chungnam National University Hospital, 282-Munhwa-ro, Jung-Gu, Daejeon 301-721, Korea, Tel.: 82-42-280-7702; Fax: 82-42-280-7932; e-mail: im1177@hanmail.net

Abstract: Androgens are important hormones that influence sebum production from the sebaceous glands. Human facial skin can be categorized as *T*- and *U*-zones, which are areas with high and low levels of sebum secretion, respectively. This study was performed to investigate whether there are topographical differences in androgen receptor (AR) expression related to regional variations in facial sebum secretion. The results of *in vivo* analysis indicated a statistically significant increase in AR expression in the sebaceous gland *T*-zones compared with the *U*-zones. *In vitro* experiments using human primary sebocytes also yielded similar results, with higher levels of AR protein and mRNA expression in *T*-zones. The results of this study suggested that differences in androgen susceptibility may be an important factor influencing regional differences in sebum production in human facial skin.

Key words: androgens – face – sebaceous glands – sebum

Accepted for publication 28 November 2013

Systemic Administration of Platelets Incorporating Inactivated Sendai Virus Eradicates Melanoma in Mice

Tomoyuki Nishikawa[1], Li Yu Tung[1] and Yasufumi Kaneda[1]

[1]Division of Gene Therapy Science, Osaka University Graduate School of Medicine, Osaka, Japan [Q1]

Tumor microenvironments include a number of fibrin clots due to the microbleeding caused by cancer cell invasion into blood vessels, which suggests the potential utility of a platelet vector for systemic cancer treatment. We previously reported that inactivated Sendai virus (hemagglutinating virus of Japan; HVJ) envelope (HVJ-E) activates anti-tumor immunity and induces cancer cell-selective apoptosis. The hemagglutination activity that blocks the systemic administration of HVJ-E was dramatically attenuated by incorporation into platelets. Platelets incorporating HVJ-E (PH complex) were then injected into the tail veins of B16F10 melanoma-bearing mice. The PH complex primarily accumulated in tumor tissues and caused the significant accumulation of various immune cells in the tumor bed. Injections of the PH complex to the melanoma-bearing mouse significantly reduced the tumor size, and the tumor growth was ultimately arrested. Secretion of the chemokine regulated upon activation normal T-expressed and presumably secreted (RANTES) was upregulated following PH stimulation. The RANTES-depletion in melanoma-bearing mice significantly attenuated the cytotoxic T lymphocyte activity and led to a dramatic abrogation of the mouse melanoma suppression induced by the PH complex. Thus, a platelet vector incorporating viral particles, a Trojan horse for cancer treatment, will provide a new approach for cancer therapy using oncolytic viruses.

Received 21 February 2014; accepted 1 July 2014; advance online publication 00 Month 2014. doi:10.1038/mt.2014.128

INTRODUCTION

Although there have been significant advances in the field of cancer treatments in the past decades, there are still some limitations with regard to the selectivity of anticancer reagent delivery to cancer cells and the tumor microenvironment. Methods for the cancer-selective delivery of therapeutic molecules have been desired since the concept of targeted drug delivery was proposed by Paul Ehrlich as a "magic bullet" in 1906.[1] One approach, passive targeting, is based on the enhanced permeability and retention (EPR) effect. Because the structure of the tumor vasculature is immature and leaky,[2] small (less than 100 nm in diameter) drug delivery vectors are believed to reach tumor cells by passing through the spaces between endothelial cells. This concept has been generally applied to non-viral vectors. Recently, mesenchymal stem cells[3] have been used as tumor-targeting vehicles based on the finding that these cells are recruited to tumor tissues, most likely through the action of chemokines produced by the tumor tissue. A non-pathogenic obligate anaerobic bacterium, *Bifidobacterium longum*, has been shown to specifically accumulate in tumor tissues after systemic delivery.[4] The specific accumulation of this bacterium occurs due to the anaerobic conditions of tumor tissues. These results highlight the importance of the particular characteristics of the tumor microenvironment for achieving specific delivery of therapeutic molecules to tumors. When examining the characteristics of the tumor microenvironment, Matsumura *et al.* proposed the utility of cancer stromal-targeting therapy using an anti-fibrin antibody[5] because these authors found many areas of blood coagulation in tumor tissues due to microhemorrhaging caused by tumor invasion into tumor blood vessels.

Based on the observation of extensive blood coagulation in the tumor microenvironment, we hypothesized that a platelet vector could specifically target tumor tissues. Platelets have a physiologically important role in the removal of foreign materials from blood.[6] Based on this characteristic, platelets have been reported to take up a variety of particles *in vivo*, such as liposomes and viral particles.[6,7] Therefore, we attempted to incorporate an inactivated Sendai virus (HVJ; hemagglutinating virus of Japan) particle termed HVJ-envelope (HVJ-E) into a platelet vector.[8] The intratumor injection of HVJ-E alone strongly induced an anti-tumor immune response; however, a limitation of HVJ-E is that it cannot be administered systemically due to the agglutination of erythrocytes by HN (hemagglutinin) glycoproteins on the envelope.[9]

Here, we developed a novel cancer-targeting vector based on platelets, and we demonstrated the utility of an HVJ-E-incorporating platelet vector in cancer immunotherapy.

RESULTS

Platelet as a vector; infusion and release of HVJ-E and fluorescent particles

First, we examined whether HVJ-E particles could be infused into platelets. For this purpose, we determined the conditions

Correspondence: Yasufumi Kaneda, Division of Gene Therapy Science, Osaka University Graduate School of Medicine, 2-2 Yamada-oka, Suita, Osaka Japan. E-mail: kaneday@gts.med.osaka-u.ac.jp

necessary to infuse particles into platelets using FITC-beads. Murine platelets isolated from fresh blood were incubated with the beads at 37 °C for 2 hours, and then washed with PBS. Subsequently, numerous FITC-beads were observed in the platelets (**Figure 1a**). Next, using the same conditions, HVJ-E was also incubated with the platelets. Using electron microscopy, HVJ-E particles were detected in the platelets (**Figure 1b**). Immunofluorescence analysis confirmed that HVJ-E particles were infused inside the mouse platelets (with Triton X-100 treatment) (**Supplementary Figure S1a**). Additionally, human platelets successfully incorporated HVJ-E particles (**Supplementary Figure S1b**).

Next, we tested whether the infused HVJ-E particles were released from the platelets by stimulation with thrombin. First, we determined the thrombin concentration required to release SPHERO fluorescent particles that were previously infused into platelets. We found that a thrombin concentration greater than 1 U/ml was necessary for the release (**Figure 1c**). For platelets infused with HVJ-E, the viral particles were released from the platelets at a thrombin concentration of 100 U/ml (**Figure 1d**). Additionally, thrombin activity was high enough to specifically activate the PH complex in B16F10 tumor tissue whereas the thrombin activity was hardly detected in plasma. (**Supplementary Figure S1c**). These data indicate that HVJ-E particles could be infused into platelets to form PH complexes and could be released by platelet activation via thrombin stimulation.

Targeting tumor tissue in tumor-bearing mice via the systemic administration of the PH complex

The disadvantage of HVJ-E is that its systemic delivery is limited due to the hemagglutination caused by the HN protein. The injection of HVJ-E particles into the blood-stream directly can cause the agglutination of red blood cells. To avoid the coagulation caused by systemic administration, HVJ-E particles were infused in a platelet vector. The free HVJ-E particles or HVJ-E particle attached to the surface of platelet vectors were measured by a hemagglutinating assay (HA). The hemagglutinating activity of HVJ-E disturbs the systemic administration HVJ-E. When HVJ-E was mixed with chicken erythrocytes, hemagglutination was induced (H100 and H1000) (**Figure 2a**). However, after the PH complexes were washed twice with PBS, the hemagglutination activity of the

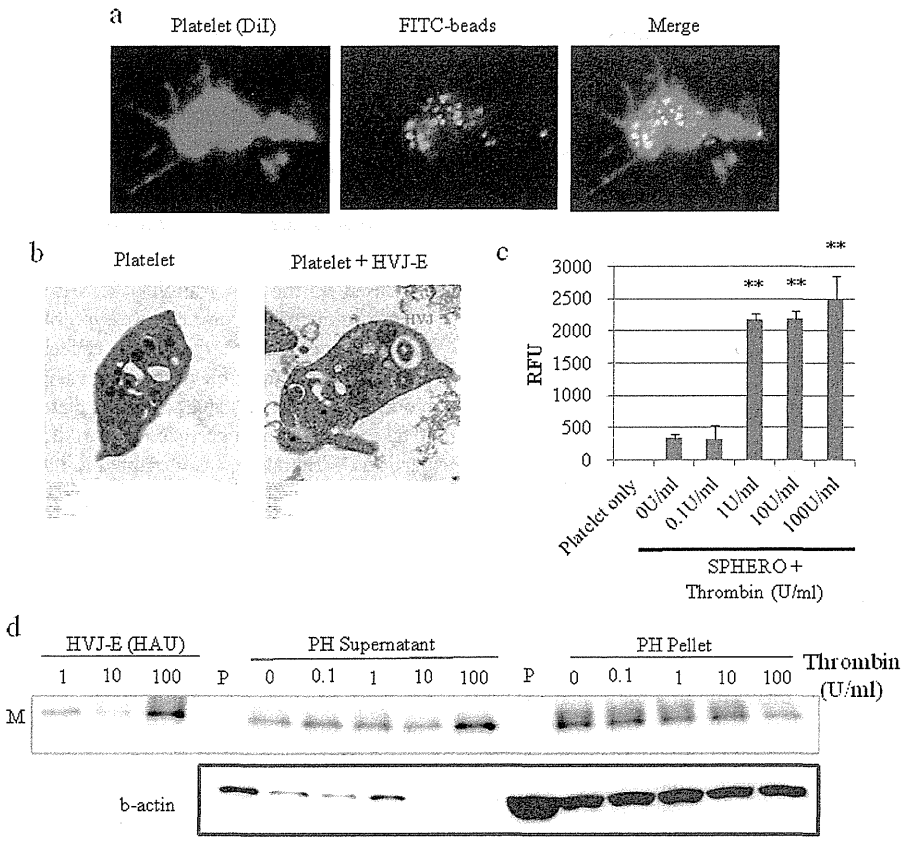

[Q2] Figure 1 Infusion and release of HVJ-E or fluorescent particles from platelets. (**a**) Infusion of FITC-beads (green) into platelets (red). Platelet membrane was stained with DiI (di-alkyl indocarbocyanine). (**b**) Transmission electron microscopic analysis of HVJ-E-infused platelets (8,000×). (**c**) Fluorescence intensity measurements of SPHERO fluorescent particles released from thrombin-stimulated SPHERO/platelet complexes. The data are shown as the mean ± SEM of four independent experiments. $^{**}P < 0.01$ (versus 0U/ml). (**d**) Western blot analysis of HVJ-E M (matrix protein of HVJ) protein after the thrombin stimulation of PH complexes. HVJ-E samples from 1 to 100 HAU (haemagglutinating units) were loaded as standard samples. The PH supernatant contained the released HVJ-E particles, and the PH pellet contained the HVJ-E particles remaining inside the platelets after thrombin stimulation. In sample P (platelets only), no thrombin was added.

PH complexes was dramatically decreased and largely undetectable (**Figure 2a**). HVJ-E particles localized to the blood vessels (PH1), whereas some HVJ-E particles were dispersed into the tumors (PH2) (**Figure 2b**).

Next, PH complexes were injected into the tail veins of B16F10 melanoma tumor-bearing mice. The colocalization of HVJ-E particles with activated platelets was observed only in the PH-treated tumors (**Figure 3a**). No PH complexes were found in other normal organs such as the liver, spleen and kidney (data not shown). Fibrin clots were consistently observed in B16F10 tumor groups (**Figure 3b**), and large numbers of activated platelets (CD62P) that colocalized with the fibrin clots in the PH-treated tumors were also observed. Additionally, tumor blood vessels were stained with FITC-albumin. Collectively, these observations indicate that the PH complexes injected into the mouse tail veins successfully reached the tumor vessels and were trapped by fibrin clots and that some complexes appeared to be associated with tumor cells.

In vivo F10 tumor suppression by PH treatment

PH complexes were injected five times into the tail veins of B16F10 melanoma tumor-bearing mice. The tumor size in the PH complex-treated group was significantly reduced (**Figure 4a**). Mice in the platelet-, HVJ-E- and NaCl-treated groups began dying after approximately 18 days, whereas all PH-treated mice were alive through 40 days (**Supplementary Figure S2**). The accumulation of immune cells, such as $CD4^+$ T cells, $CD8^+$ T cells (**Figure 4b,c**), NK cells (CD49b), and DCs (CD11c) (**Supplementary Figure S3a,b**), was observed in the PH complex-treated B16F10 tumors at 48 hours after the fifth injection.

Cytotoxicity of the PH complex or HVJ-E against cancer cells and tumor endothelial cells

The cytotoxicity of the PH complex and HVJ-E against cancer cells and tumor endothelial cells (TECs) from mouse F10 melanoma tissues was examined using an *in vitro* cell proliferation assay. PH complexes (different amounts of HVJ-E, from 100 to

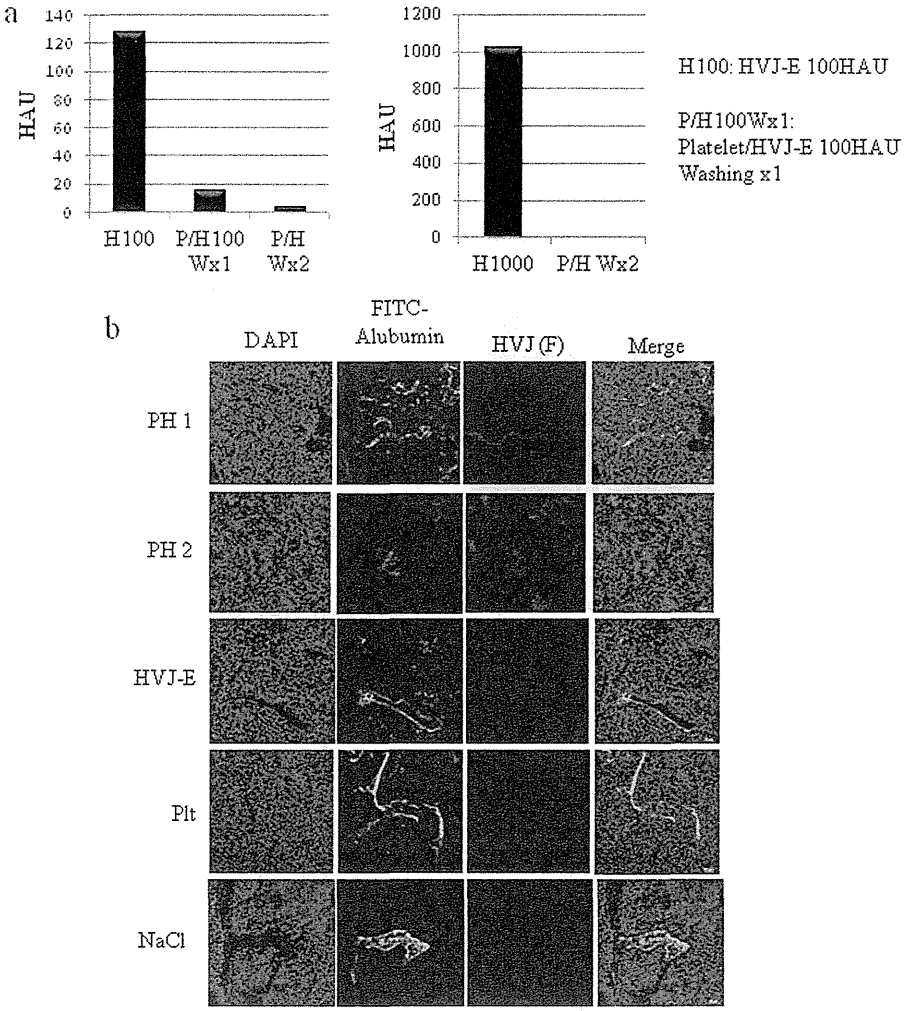

Figure 2 HA assay of PH complexes. (**a**) The hemagglutinating activity of the PH complexes (containing 100 or 1,000 HAU of HVJ-E) was reduced by washing with buffer (washing once or twice). (**b**) Tumor tissue sections were stained with FITC-albumin (green) and anti-F protein to visualize the tumor blood vessels and HVJ-E, respectively, after the administration of PH complexes (PH), HVJ-E, platelets (Plt), or NaCl solution (NaCl).

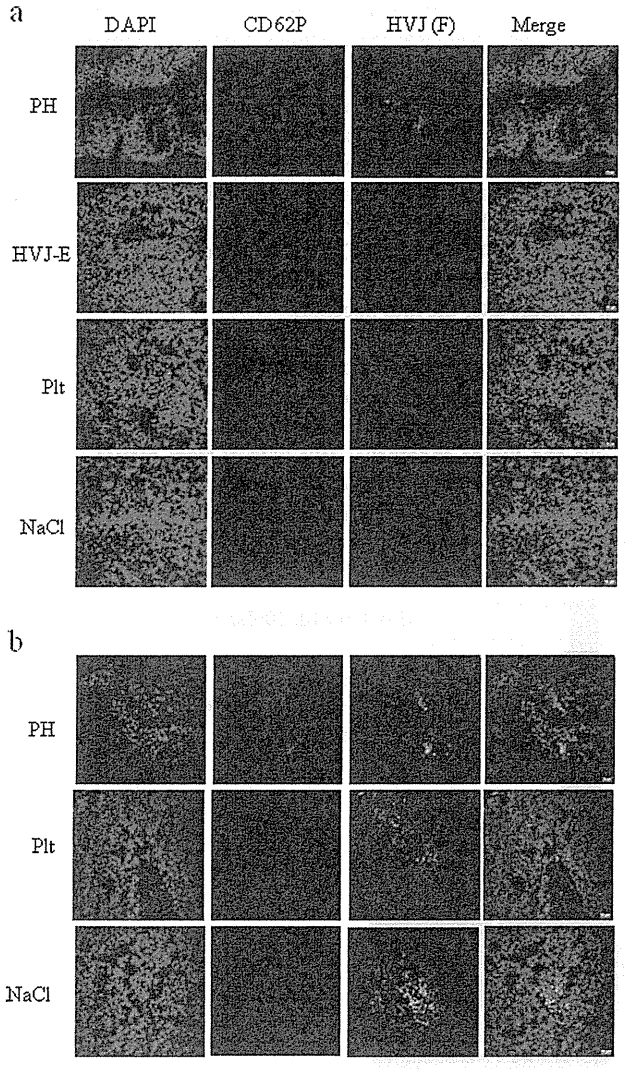

Figure 3 The administration of PH complexes (PH), HVJ-E, platelets (Plt), or NaCl solution (NaCl) to B16F10 melanoma-bearing mice and the accumulation of delivered HVJ-E particles in tumor tissues. (**a**) Tumor sections were stained with anti-CD62P (red) and anti-F protein (green) to visualize the activated platelets and HVJ-E localization, respectively. (**b**) Tumor sections were stained with anti-CD62P (red) and anti-fibrin (green) to visualize the activated platelets and fibrin localization, respectively.

2,000 HAU, were infused into the same number of platelets) and HVJ-E were added to B16F10 (mouse melanoma) cells and TECs (**Figure 5a,b**). PH complexes at higher concentrations suppressed the proliferation of the B16F10 cancer cells, but not the TECs, 48 hours after transfection. PH complexes and HVJ-E were also added to human pancreatic carcinoma cells (PC3), human umbilical vein endothelial cells (HUVECs) and human aortic endothelial cells (HAECs). Only the proliferation of PC3s was suppressed, and the proliferation of HUVECs and HAECs was not affected (**Supplementary Figure S4a–c**). B16F10 cells were treated with PH complexes after transfection with siRNA for RIG-I or MAVS. A proliferation assay of PH complex-treated B16F10 cells showed that cell death caused by the PH complexes was significantly suppressed by either RIG-I or MAVS siRNA, but not control siRNA (**Supplementary Figure S5**). This result indicates that similar to HVJ-E,[10] PH complexes induced cell death through the RIG-I/MAVS pathway.

The contribution of the HVJ-E-induced chemokine, RANTES/CCL5, to tumor suppression by activated anti-tumor immunity

Cytokine and chemokine arrays were used to identify the factors that contributed to the suppression of PH-treated tumors. TEC isolated from B16F10 tumors and B16F10 cells were stimulated with PH complexes, and RANTES was the most highly secreted chemokine in both cases (**Figure 6a,b**). PH complexes also stimulated HUVECs to secrete RANTES, IP-10 and IL-6 (**Supplementary Figure S6a**). RANTES secretions from TECs and F10 cells were also measured (**Supplementary Figure S6a,b**). IP-10 secretions from TECs and F10 cells was detected but there was no significant difference among any of the groups (NC, platelet, HVJ-E, and PH). IL-6 secretion from TEC and F10 cells was not detected. The HVJ-E and PH groups, but not the platelet group, showed the induction of RANTES secretion, which indicated that the HVJ-E particles were the sole inducer of RANTES.

A RANTES-neutralizing antibody was administered with the PH complexes to mice bearing B16F10 melanomas to verify the tumor suppression effect. The suppression effect of the PH complexes was abrogated by the RANTES-neutralizing antibody (**Figure 6c**). The expression of RANTES in melanoma tissue was enhanced by the PH complexes and was abolished in the RANTES-neutralizing antibody group (**Figure 6d**). Mice in the RANTES-depletion group started dying after approximately 18 days, similar to the NaCl-injected group, whereas all PH-treated mice remained alive through 40 days (**Supplementary Figure S7**).

Robust production of interferon (IFN)-γ from mouse splenocytes was achieved in response to melanoma stimulation, suggesting the activation of CTLs specific to the melanoma cells by the systemic administration of the PH complexes to B16F10-bearing mice (**Figure 7a**). An ELISPOT (IFN-γ) assay was performed using mouse splenocytes stimulated with B16F10 or MSC-1 (mesenchymal stromal cell from C57BL/6 mouse) cells (**Supplementary Figure S8a**). The splenocytes isolated from PH-treated F10-bearing mice specifically responded to the B16F10 cells, but not the MSC-1 cells. Anti-CD4 (clone GK1.5) or anti-CD8 (clone 53–7.62) antibodies were injected into the melanoma-bearing mice to deplete $CD4^+$ or $CD8^+$ T cells, respectively. In both the CD4- and CD8-depleted groups, the tumor suppression by the PH complex was significantly abrogated compared with the control IgG-injected group (**Figure 7b,c**). NK cells were also depleted by the injection of an anti-asialo GM1 antibody into B16F10-bearing mice. The NK cell-depleted group had significant attenuation of tumor suppression by the PH complex compared with the control IgG-injected group (**Figure 7d**). These results strongly suggest that both $CD4^+$ and $CD8^+$ T cells are necessary to activate CTLs to respond to B16F10 cells and that NK cells also contribute to tumor killing following PH complex treatment.

A CTL assay (^{51}Cr-release assay) using mouse splenocytes isolated from B16F10-bearing mice was performed

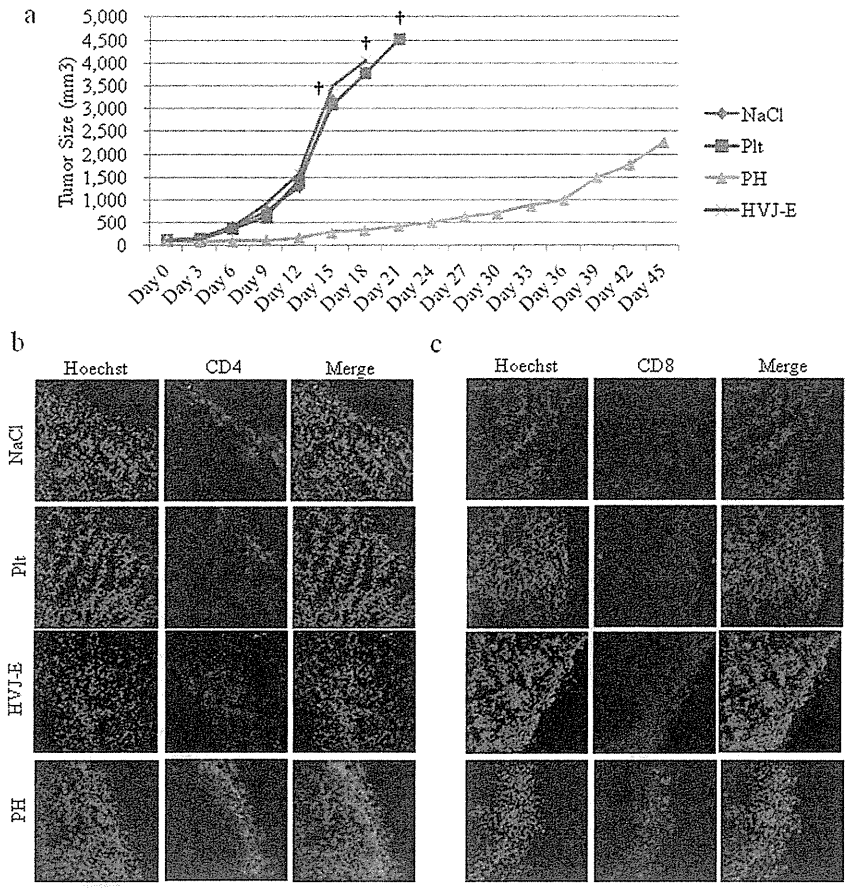

Figure 4 Suppression of tumor growth by PH complex treatment in B16F10 melanoma-bearing mice and the accumulation of immune cells in the tumor. (**a**) Tumor growth curve of B16F10 melanoma-bearing mice treated with PH complexes (PH), HVJ-E, platelets (Plt), or NaCl solution (NaCl). The data are shown as the mean ± SEM of four animals per group. †The date when the number of mouse in the group became less than 2. (**b**,**c**) B16F10 tumor tissue sections from tumor-bearing mice treated with PH complexes (PH), HVJ-E, platelets (Plt) or NaCl solution were stained with anti-CD4 (red) and anti-CD8 (red) antibodies to visualize the localization of $CD4^+$ and $CD8^+$ T cells, respectively, in the tumor tissues.

(**Supplementary Figure S8b**). The splenocytes from the PH-treated mice demonstrated specific cytotoxicity against B16F10 cells, but not against MSC-1 cells. Collectively, these observations suggest that the PH complex induces anti-tumor immunity via the activation of both CTLs and NK cells and that RANTES plays a major role in the promotion of anti-tumor immunity.

In summary, as illustrated in **Figure 8**, systemically administered PH complexes targets the fibrin clots that dominantly present in tumor blood vessels and presumably release HVJ-E after activation in the fibrin clots. In not only B16F10 but also B16BL6 (mouse melanoma) and LL/2 (mouse Lewis lung carcinoma) tumor tissue sections, many thrombi (CD41-positive blood clots) were observed in the tumor vasculatures (stained with CD31 antibody) (**Supplementary Figure S9a**). The three different tumor tissue samples were collected at three different time points/tumor sizes (7 days/5 mm, 14 days/10 mm and 21 days/15 mm). Staining of the tumor sections with an anti-fibrin antibody revealed fibrin clots in all sample sections (**Supplementary Figure S9b–d**). Therefore, the systemic injection of PH complexes can induce similar anti-tumor effects in other murine tumor models. The HVJ-E particles, which were released from activated platelet vectors, induced the secretion of RANTES from TECs and B16F10 cells. Collectively, the combination of HVJ-E and RANTES accelerates tumor regression by enhancing anti-tumor immunity.

DISCUSSION

Here, we demonstrated that the systemic administration of a platelet vector containing HVJ-E dominantly accumulates in tumor tissues and results in significant tumor regression in melanoma-bearing mice. Platelets were the only factor that was not detected by CD62P immunostaining in the tumor tissues; however, the PH detected by CD62P was well merged with the fibrin clots (**Figure 2b**). This finding suggests that PH was likely activated within the tumors to release HVJ-E from the platelets into the tumor microenvironment. Notably, some, but not all, of the PH overlapped with FITC-albumin. This result suggests that some HVJ-E may escape from tumor vessels to directly associate with the tumor cells. As shown in **Supplementary Figure S4a**, PH reduced the survival of cultured cancer cells. We previously reported that HVJ-E directly induced apoptosis in cultured cancer cells by viral RNA fragment-mediated RIG-I activation. The PH complex appears to enhance direct

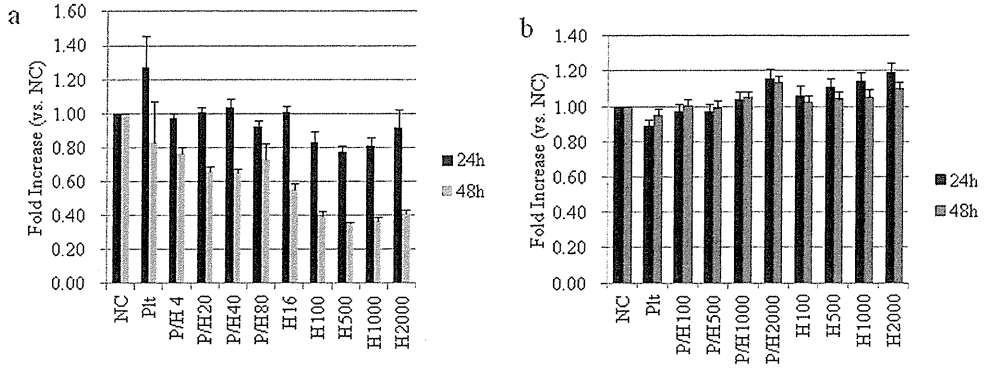

Figure 5 Proliferation assay of B16F10 melanoma cells and isolated TECs from mouse F10 melanoma tumors. Different concentrations of HVJ-E (from 4 or 100 to 2,000 HAU) were infused into the same number of platelets (5.0×10^6 platelets) to construct various PH complexes. The PH complexes and different concentrations of HVJ-Es were added to (**a**) B16F10 or (**b**) TECs. The survival rates of the cells were measured. The data are shown as the mean ± SEM of four independent analyses.

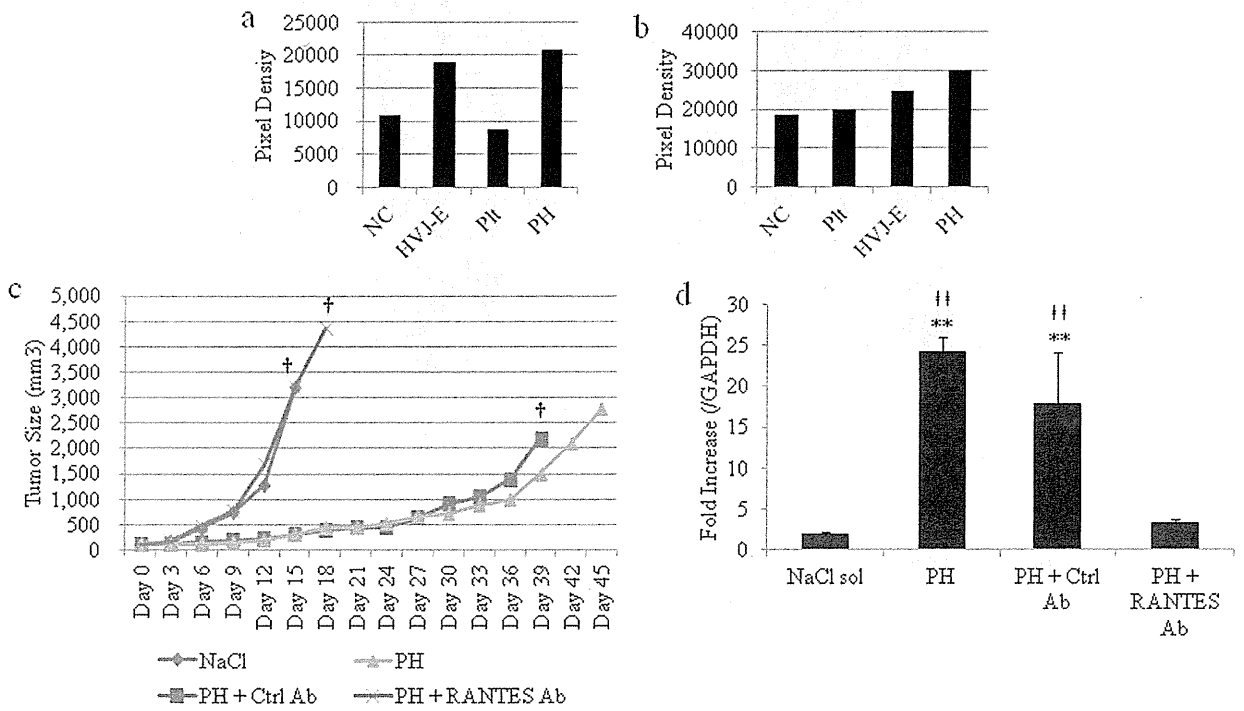

Figure 6 HVJ-E-induced RANTES production contributed to tumor suppression. (**a**,**b**) Chemokine and cytokine arrays of PH-treated TECs isolated from (**a**) tumors and (**b**) B16F10 cells. (**c**) Tumor growth curves of B16F10 melanoma-bearing mice treated with PH complexes (PH), PH complexes + RANTES-neutralizing antibody (PH + RANTES Ab), PH complexes + control IgG (PH + Ctrl Ab) or NaCl solution (NaCl). †The date when the number of mouse in the group became less than 2. The data are shown as the mean ± SEM of four animals per group. (**d**) RT-PCR of RANTES mRNA level in B16F10 tumor tissues. The F10 tissue samples were collected 48 hours after three injections. The data are shown as the mean ± SEM of four independent analyses. ‡‡$P < 0.01$ (versus PH + RANTES-neut ab); **$P < 0.01$ (versus NaCl).

tumor cell killing via the same signaling pathway utilized by HVJ-E. In tumor-bearing mice, the direct killing of melanoma cells may also contribute to PH-mediated tumor suppression and the enhancement of anti-tumor immunity. However, when melanoma-bearing mice are treated with PH, the contribution of the direct cancer cell-killing activity of PH to the suppression of melanoma growth may be much less than that of its anti-tumor immune activity as the number of HVJ-E particles (189 HAU/mouse) introduced into the tumor-bearing mice was much smaller than the number of HVJ-E particles needed for the direct killing of cancer cells.

PH complexes successfully delivered HVJ-E particles and induced RANTES secretion, which enhanced the inhibition of tumor growth. In the *in vitro* assay, HVJ-E was released from the platelets via thrombin treatment. Although we had no clear evidence that HVJ-E was also released from platelets in the tumor tissues, activated platelets were detected with CD62P in the tumor tissues only when they contained HVJ-E. However, the reason for

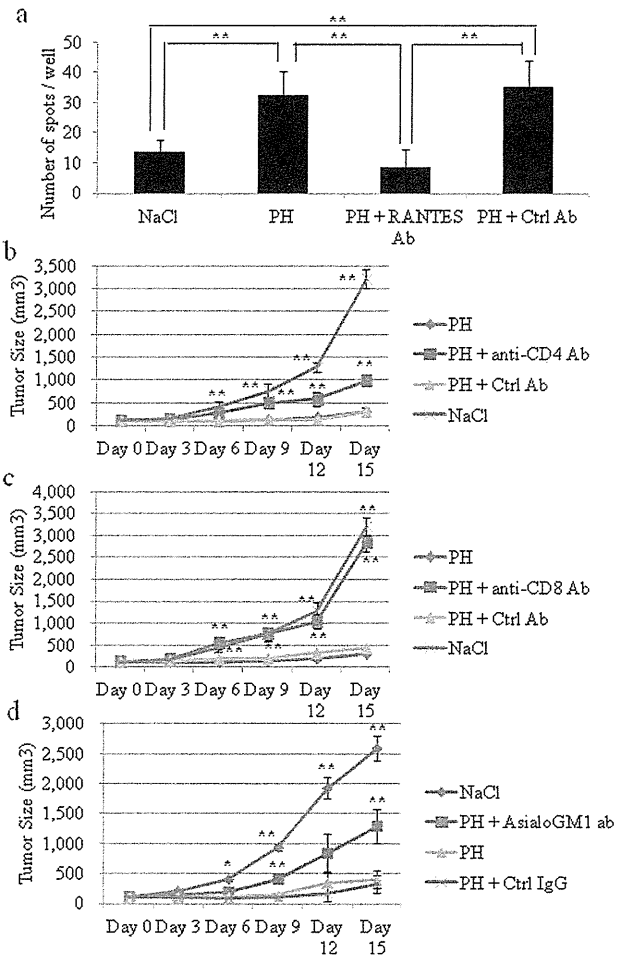

Figure 7 Induction of the anti-tumor immune response by T cells and NK cells in PH-treated tumor-bearing mice. (**a**) ELISPOT assay. Induction of IFN-γ from splenocytes isolated from PH-treated F10 tumor-bearing mice after 48 hours of incubation with or without B16F10 cells. The data are shown as the mean ± SEM of six independent analyses. $^{**}P < 0.01$. (**b–d**) Tumor sizes of (**b**) CD4$^+$ T cell-, (**c**) CD8$^+$ T cell-, or (**d**) NK cell-depleted B16F10-bearing mice. The data are shown as the mean ± SEM of four animals per group. $^{*}P < 0.05$ (versus PH), $^{**}P < 0.01$ (versus PH).

the activation of platelets containing HVJ-E *in vivo* remains to be elucidated.

Our results also demonstrated that platelets possess the ability to suppress the hemagglutination activity of HVJ-E, which is a limitation of HVJ-E. The intratumor injection of HVJ-E is being clinically tested in Japan for the treatment of patients with melanoma and prostate cancer. The systemic administration of HVJ-E using platelets will expand the applications for HVJ-E in cancer therapy.

After five injections of PH complexes or NaCl into B16F10-bearing mice, the serum was isolated and an antibody to HVJ-E was measured by mouse anti-Sendai virus (HVJ) IgG ELISA. The PH treatment group showed evidence of the production of anti-Sendai virus IgG (data not shown). However, we already reported that even in the presence of anti-HVJ antibodies, gene transfer using HVJ-E is not suppressed.[11,12]

In this study, we revealed that the RANTES chemokine, one of the major chemokines, induces a strong anti-tumor immune response. RANTES (CCL5), which is a member of the CC chemokine family, has strong chemotactic activity toward multiple immune cells, such as eosinophils, basophils, mast cells, monocytes, CTLs, naïve CD4$^+$ T cells and memory CD45RO$^+$ T cells.[13–16] Several studies have investigated the efficacy of expressing RANTES for the promotion of anti-tumor immunity. These studies showed that the ectopic, intratumoral expression of RANTES attracted and activated tumor-specific and tumor-non-specific immune cells, such as DCs, CD4$^+$ T cells, CD8$^+$ T cells, and NK cells.[17–19] PH complexes reached the fibrin-rich area of the tumor and released HVJ-E particles. Subsequently, the released HVJ-E particles stimulated the secretion of RANTES from the endothelial and/or tumor cells, and consequently, the secreted RANTES contributed to attracting anti-cancer immune cells.

However, when only recombinant RANTES was injected into the melanoma mass, tumor suppression was not significantly achieved (data not shown). Several studies have reported that RANTES exhibits pleiotropic activities in tumor development: it not only attracts immune cells to the tumor tissue, but also promotes tumor proliferation and invasion. Other studies have reported the expression of RANTES in primary human tumors, such as renal, prostate, breast and ovarian cancers, and melanoma.[20–26] In the RANTES-expressing MCF-7 human breast cancer cell line, RANTES promoted cell proliferation by an mTOR-dependent process.[27] Thus, the roles of RANTES in tumor biology remain somewhat controversial and are not fully understood. Therefore, our study of melanoma treatment using the PH complex shows that the presence of HVJ-E in melanoma tissue is likely to be essential for enhancing anti-tumor immunity *in vivo*, in addition to inducing the secretion of RANTES.

The incorporation of anti-cancer compounds and other viral particles into platelet vectors appears to be feasible. Although solving the problems related to the mass production and long-term storage of platelets for clinical use is important, we have already succeeded in incorporating HVJ-E into freeze-dried platelets. As shown in **Supplementary Figure S1b**, HVJ-E particles were incorporated into human platelets, which indicate the clinical utility of the PH complex.

Thus, platelet vectors are promising tools for cancer treatment with minimum toxicity.

MATERIALS AND METHODS

Virus. HVJ (VR-105 parainfluenza1 Sendai/52, Z strain) was purchased from the American Type Culture Collection (ATCC; Manassas, VA) and amplified in the chorioallantoic fluid of 10- to 14-day-old chick eggs and purified by centrifugation, as previously described.[28,29]

Mice. Female C57BL/6N mice and Fox Chase SCID C.B-17/Icr-scid/scidJcl mice were purchased from Clea Japan (Tokyo, Japan) and were maintained in a temperature-controlled, pathogen-free room. All the animals were handled according to the approved protocols and guidelines of the Animal Committee of Osaka University (Suita, Japan).

Platelet purification and infusion of virus and fluorescent particles. Anticoagulated mouse blood was centrifuged at 200*g* for 3 minutes, and the upper, platelet-rich plasma (PRP) was collected. The PRP was centrifuged at 200*g* for 3 minutes, and the platelets were resuspended in modified

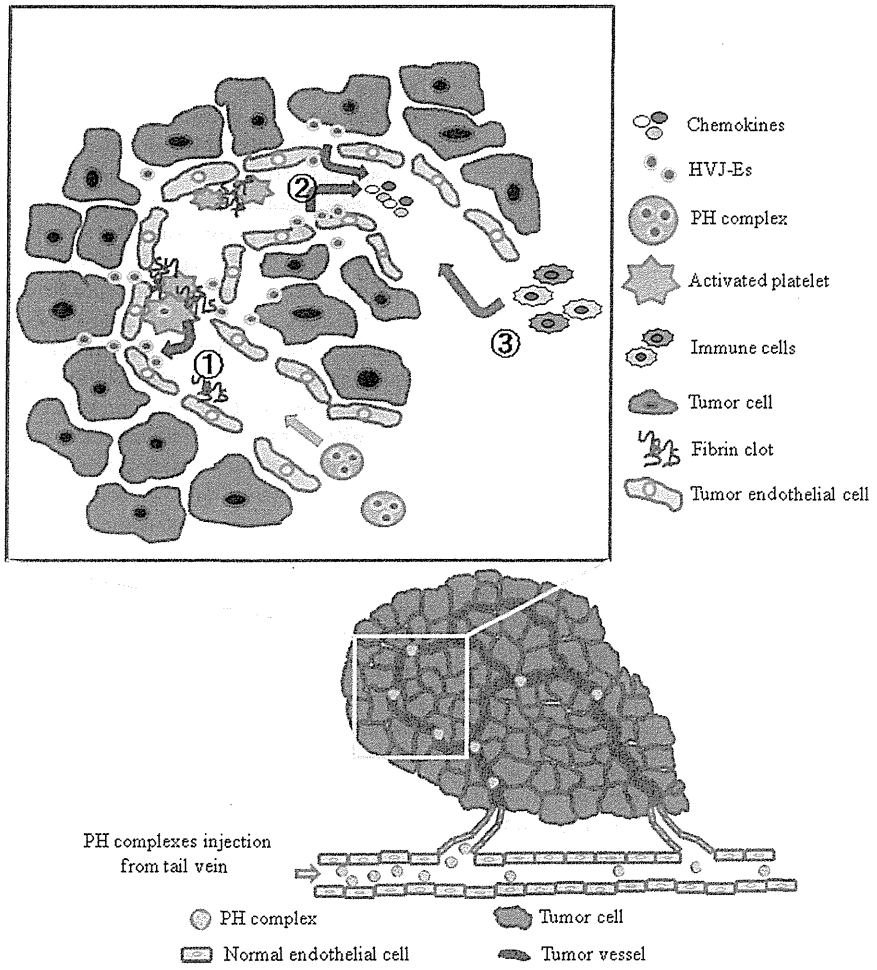

Figure 8 Model depicting the mechanism by which the PH complex targets and induces chemokine production in F10 tumor tissues. The PH complex is inactive in normal blood vessels; however, when it interacts with fibrin clots in tumor vessels, the complex begins to release the HVJ-E particles (1), which induces TECs or cancer cells to secrete chemokines, mainly RANTES (2). The cytokines recruits immune cells to the tumor tissue (3), which enhance anti-tumor immunity.

[Q3] Tyrode's buffer (134 mmol/l NaCl, 2.9 mmol/l KCl, 0.34 mmol/l Na_2HPO_4, 1 mmol/l $MgCl_2$, 10 mmol/l HEPES, and 5 mmol/l D-glucose, pH 7.4). Prostaglandin I_2 sodium salt was added to the PRP (1 pg/ml final concentration) and incubated for 2 minutes. The platelets were washed by the addition of 1 ml of Tyrode's buffer. Human platelets were isolated using the same procedure as mouse platelets from human blood that was donated by a human volunteer.

HVJ-E, Fluoresbrite plain YG (0.1 μm) microparticles (Polysciences, Warrington, PA) or SPHERO fluorescent particles (0.04–0.06 μm; Spherotech, Lake Forest, IL) were incubated with the platelets at 37 °C for 2 hours and were washed twice with modified Tyrode's buffer.

Transmission electron microscopy. Platelets and PH complexes were fixed with 2.5% glutaraldehyde in 0.1 mol/l phosphate buffer (pH 7.4) at 4 °C and were post-fixed in 1% OsO_4 solution at 4 °C for 1 hour. The samples were dehydrated in a graded ethanol series and embedded in Quetol 812 epoxy resin (Nissin EM, Tokyo, Japan). Ultrathin sections (80 nm) were cut with a Reichert ultramicrotome (Ultracut E, Leica Microsystems K.K., Tokyo, Japan), stained with uranyl acetate and lead citrate and examined under a Hitachi H-7650 electron microscope (Hitachi, Tokyo, Japan).

Thrombin stimulation of HVJ-E or fluorescent/platelet complex. HVJ-E/platelet complexes were stimulated with thrombin (GE Healthcare UK Limited) for 4 hours at 37 °C and centrifuged at 200*g* to collect the platelets. The supernatant, which contained the released HVJ-E particles, was centrifuged at 20,400*g*. The platelets and released HVJ-E particle samples were analyzed by Western blot.

Fluorescent particles (SPHERO/platelet complexes) were stimulated with thrombin for 14 hours at RT and centrifuged at 200*g*. The fluorescence intensity of the supernatant was measured using a Mithras LB 940 (Berthold Japan K.K., Tokyo, Japan).

Western blot analysis. The samples were subjected to SDS-PAGE on 12% gels, and the proteins were transferred to Immobilon-P transfer membranes (Millipore, Billerica, MA). To detect the proteins, anti-M (Hokkaido System Science) or anti-β-actin (Sigma-Aldrich Japan, Tokyo, Japan) immunoglobulin G (IgG) was used as the primary antibody. ECL horseradish peroxidase-conjugated donkey anti-rabbit IgG (GE Healthcare UK) was used as a secondary antibody for the detection of M (matrix protein of HVJ), and ECL horseradish peroxidase-conjugated sheep anti-mouse IgG (GE Healthcare UK) was used as a secondary antibody for the detection of

β-actin. The ECL Western Blotting Detection Reagent (GE Healthcare UK) was used to detect the signal for each protein.

Hemagglutination (HA) assay. PH complexes were serially diluted in PBS in a 96-well U-bottom plate. A 50-μl aliquot of a suspension of chicken red blood cells (0.5% RBCs) (Nacalai Tesque, Kyoto Japan) was then added to each well, and the samples were incubated at 4 °C for 16 hours. The agglutination titer was determined as the last dilution at which agglutination was detected.

Cell culture and proliferation assay. B16F10 (mouse melanoma), B16BL6 (mouse melanoma), LL/2 (mouse Lewis lung carcinoma) and MSC-1 (mouse mesenchymal stromal cells) cells were maintained in Dulbecco's modified Eagle's medium (Nacalai Tesque) Murine splenocytes were maintained in RPMI-1640 medium (Nacalai Tesque). All media were supplemented with 10% FBS (BioWest, Nuaillé, France), 100 U/ml penicillin and 0.1 mg/ml streptomycin (Penicillin-Streptomycin Mixed Solution, Nacalai Tesque). β-Mercaptoethanol (4 ng/ml) was added to the medium for the splenocyte culture. B16F10 cells (1.0×10^3 cells/well) were seeded into 96-well plates, and HVJ-E or PH complexes were added to the wells. After 24 or 48 hours of incubation, 20 μl of Cell Titer 96 AQueous One Solution (Promega, Madison, WI) was added to each well to measure the viability of the cancer cells. The plates were incubated at 37 °C for 2 hours, and the absorbance was measured at a wavelength of 490 nm according to the manufacturer's instructions.

In vivo ***tumor volume measurement and RANTES depletion.*** Viable B16F10 melanoma cells (1.0×10^6 cells) were resuspended in 50 μl of PBS and were intradermally injected into the backs of female C57BL/6N mice. When each tumor had grown to 3–5 mm in diameter, the mice were treated with an intravenous tail injection of platelets (2.5×10^5), HVJ-E (1.89×10^9 particles), PH complexes (1.89×10^9 particles of HVJ-E infused into 2.5×10^7 platelets, for a total volume of 50 μl), or PBS on days 0, 3, 6, 9 and 12. The tumor volume was measured in a blinded manner using slide calipers and was calculated using the following formula: tumor volume (mm^3) = length × $(width)^2/2$. To deplete RANTES, an anti-RANTES antibody (ab9915; Abcam, Cambridge, MA) was administered intravenously at the time of PH complex administration. Rabbit IgG (R&D Systems, Minneapolis, MN) was used as a control for the anti-RANTES antibody.

Immunostaining of immune cells in F10 tumor tissues. The PH complex-treated and other F10 melanoma tumor sections were fixed with 4% paraformaldehyde solution and blocked with 3% BSA. The sections were stained with anti-CD4 and anti-CD8 primary antibodies (Sigma-Aldrich Japan). The secondary antibodies included an Alexa Fluor 488-conjugated rabbit anti-mouse IgG (Life Technologies Corporation, Carlsbad, CA). The sections were mounted in Vectrashield mounting medium (Vector Laboratories, Burlingame, CA) and imaged with a confocal laser microscope (Radiance 2100; Bio-Rad Laboratories, Drive Hercules, CA) equipped with the Laser Sharp 2000 software program. Anti-CD62P (550289; BD Bioscieces Pharmingen, San Diego, CA) and anti-fibrin (D01P; Abnova, Taipei City, Taiwan) primary antibodies were used to detect activated platelets and fibrin, respectively, in the F10 tumor tissues.

Isolation of vascular endothelial cells from B16F10 tumors and cytokine and chemokine arrays. Tumor vascular endothelial cells were isolated from B16F10-bearing mice. The B16F10 tumor tissue was minced and enzymatically digested in PBS supplemented with 3% collagenase (Sigma-Aldrich Japan) using an orbital shaker for 30 minutes at 37 °C. The digested tissue was filtered through a 40-mm nylon mesh cell strainer (BD Biosciences, Bedford, MA). The sample was placed on top of a Percoll solution (Sigma-Aldrich Japan) and centrifuged at 400*g* for 30 minutes. The second layer, which contained endothelial cells, was transferred to a 100-mm culture dish and incubated at 37 °C in 5% CO_2 for 1.5 hours. This procedure allowed the fibroblasts and preadipocytes contained in the mixture to attach to the culture dish. The medium, which contained suspended endothelial cells, was carefully transferred to another tube. The endothelial cells were further purified using an autoMACS Pro Separator with an anti-CD105 antibody (Miltenyi Biotech, Bergisch Gladbach, Germany). The isolated ECs or B16F10 cells were seeded into six-well plates (1.5×10^6 cells/well), and platelets (2.5×10^5), HVJ-E (1.89×10^9 particles), or PH complexes (1.89×10^9 particles) were added to the medium. After 24 hours, the media were collected and used as samples for cytokine and the chemokine arrays (Proteome Profiler Panel A Array Kit; RD Systems, Minneapolis, MN). The pixel densities of the spots on the array membranes were quantified using Image Quant TL software (GE Healthcare Japan, Tokyo, Japan).

Preparation of splenocytes and ELISPOT (mouse IFN-γ) assay. Spleens were removed aseptically from PH complex-treated mice after the fifth injection. Antigen-specific IFN-γ-producing cells were identified using an enzyme-linked immunosorbence spot (ELISPOT) assay. Briefly, ELISPOT plates (IP Sterile Clear Plate, MAIPS4510; Millipore, Bedford, MA) were coated with an anti-mouse IFN-γ capture Ab (Mouse IFN-γ ELISpot Development Module; RD Systems, Minneapolis, MN). Spleen cells (2.0×10^7 cells) and mitomycin C (Nacalai Tesque)-treated B16F10 melanoma cells (2.0×10^6 cells) were co-incubated for 12 hours. The pre-stimulated spleen cells (5.0×10^5 cells) were placed onto an antibody-coated plate with B16F10 cells (2.0×10^3 cells). After 48 hours of incubation at 37 °C, the cells were removed by washing the plates, and the sites of cytokine secretion were detected using biotinylated anti-mouse IFN-γ detection Ab and streptavidin-alkaline phosphatase conjugate (ELISpot Blue Color Module). The enzymatic reaction was developed with BCIP-NBT substrate.

Depletion of CD4, CD8, and NK cells in B16F10-bearing mice. Anti-CD4 (clone GK1.5) and anti-CD8 (clone 53–7.62) antibodies were kindly provided by Murakami (Osaka University, Suita, Japan), and the anti-asialo GM1 antibody was purchased from Wako Pure Chemical Industries. To deplete the CD4 T cells, CD8 T cells, or NK cells, each antibody [anti-CD4 (200 mg), anti-CD8 (500 mg), or anti-asialo GM1 (20 mg), respectively] was administered intraperitoneally on days -1, 0, 1, 2, 4, 6, 8, 11, and 14. Rat IgG (Sigma) was used as a control for the anti-CD4 and anti-CD8 antibodies, and rabbit IgG (R&D Systems) was used as a control for the anti-asialo GM1 antibody.

Statistical analysis. The statistical analyses were conducted using the Tukey-Kramer test or Student's unpaired *t*-test, and *P* values less than 0.05 were considered statistically significant.

SUPPLEMENTARY MATERIAL

Figure S1. Immunostaining of infused HVJ-E F-protein in mouse and human platelets.
Figure S2. Survival rate of PH complex-treated B16F10-bearing mice.
Figure S3. Tumor sections were stained with anti-CD49b and CD11c to visualize the localization of NK cells and DCs.
Figure S4. Proliferation assay of HVJ-E and PH complex-treated PC3s and human endothelial cells (HUVECs and HAECs).
Figure S5. Proliferation assay of PH-treated RIG-I and MAVS siRNA-transfected B16F10 cells.
Figure S6. Human cytokine and chemokine array of PH complex-stimulated HUVEC, TEC, and B16F10 cells.
Figure S7. Survival rate of PH complex and RANTES antibody-treated B16F10-bearing mice.
Figure S8. Specific antitumor effects induced by PH complex injection into B16F10-bearing mice, analyzed by ELISPOT and ^{51}Cr-release assay.
Figure S9. Thrombus and fibrin clot localization in various tumors (B16F10, B16BL6, and LL/2).
Supplementary Materials and Methods [Q4]

ACKNOWLEDGMENTS

This work was financially supported by Grant-in-Aid for Scientific Research (B) from the Japan Society for the Promotion of Science. The authors thank Masaaki Murakami (Hokkaido University, Sapporo,

Japan) for providing anti-CD4 and anti-CD8 antibodies. The work was conducted in Suita, Osaka, Japan. The authors declare no conflict of interest.

REFERENCES

1. Ehrlich, P (1906). *Collected Studies on Immunity*. J. Wiley & sons: New York.
2. Maeda, H, Wu, J, Sawa, T, Matsumura, Y and Hori, K (2000). Tumor vascular permeability and the EPR effect in macromolecular therapeutics: a review. *J Control Release* **65**: 271–284.
3. Altaner, C, Altanerova, V, Cihova, M, Ondicova, K, Rychly, B, Baciak, L *et al.* (2014). Complete regression of glioblastoma by mesenchymal stem cells mediated prodrug gene therapy simulating clinical therapeutic scenario. *Int J Cancer* **134**: 1458–1465.
4. Taniguchi, S, Fujimori, M, Sasaki, T, Tsutsui, H, Shimatani, Y, Seki, K *et al.* (2010). Targeting solid tumors with non-pathogenic obligate anaerobic bacteria. *Cancer Sci* **101**: 1925–1932.
5. Matsumura, Y (2012). Cancer stromal targeting (CAST) therapy. *Adv Drug Deliv Rev* **64**: 710–719.
6. Male, R, Vannier, WE and Baldeschwieler, JD (1992). Phagocytosis of liposomes by human platelets. *Proc Natl Acad Sci U S A* **89**: 9191–9195.
7. Flaujac, C, Boukour, S and Cramer-Bordé, E (2010). Platelets and viruses: an ambivalent relationship. *Cell Mol Life Sci* **67**: 545–556.
8. Kaneda, Y, Nakajima, T, Nishikawa, T, Yamamoto, S, Ikegami, H, Suzuki, N *et al.* (2002). Hemagglutinating virus of Japan (HVJ) envelope vector as a versatile gene delivery system. *Mol Ther* **6**: 219–226.
9. Kaneda, Y (2012). Virosome: a novel vector to enable multi-modal strategies for cancer therapy. *Adv Drug Deliv Rev* **64**: 730–738.
10. Matsushima-Miyagi, T, Hatano, K, Nomura, M, Li-Wen, L, Nishikawa, T, Saga, K *et al.* (2012). TRAIL and Noxa are selectively upregulated in prostate cancer cells downstream of the RIG-I/MAVS signaling pathway by nonreplicating Sendai virus particles. *Clin Cancer Res* **18**: 6271–6283.
11. Kaneda, Y, Yamamoto, S., Nakajima, T (2005). *Development of HVJ Envelope Vector and its Application to Gene Therapy*. Elsevier Academic Press. [Q5]
12. Mima, H, Tomoshige, R, Kanamori, T, Tabata, Y, Yamamoto, S, Ito, S *et al.* (2005). Biocompatible polymer enhances the *in vitro* and *in vivo* transfection efficiency of HVJ envelope vector. *J Gene Med* **7**: 888–897.
13. Alam, R, Stafford, S, Forsythe, P, Harrison, R, Faubion, D, Lett-Brown, MA *et al.* (1993). RANTES is a chemotactic and activating factor for human eosinophils. *J Immunol* **150**(8 Pt 1): 3442–3448.
14. Bischoff, SC, Krieger, M, Brunner, T, Rot, A, von Tscharner, V, Baggiolini, M *et al.* (1993). RANTES and related chemokines activate human basophil granulocytes through different G protein-coupled receptors. *Eur J Immunol* **23**: 761–767.
15. Schall, TJ, Bacon, K, Toy, KJ and Goeddel, DV (1990). Selective attraction of monocytes and T lymphocytes of the memory phenotype by cytokine RANTES. *Nature* **347**: 669–671.
16. Pietrzak, A, Misiak-Tłoczek, A and Brzezińska-Błaszczyk, E (2009). Interleukin (IL)-10 inhibits RANTES-, tumour necrosis factor (TNF)- and nerve growth factor (NGF)-induced mast cell migratory response but is not a mast cell chemoattractant. *Immunol Lett* **123**: 46–51.
17. Fuentes-Beltrán, A, Montes-Vizuet, R, Valencia-Maqueda, E, Negrete-García, MC, García-Cruz, Mde L and Teran, LM (2009). Chemokine CC-ligand 5 production and eosinophil activation into the upper airways of aspirin-sensitive patients. *Clin Exp Allergy* **39**: 491–499.
18. Sallusto, F, Lenig, D, Mackay, CR and Lanzavecchia, A (1998). Flexible programs of chemokine receptor expression on human polarized T helper 1 and 2 lymphocytes. *J Exp Med* **187**: 875–883.
19. Campbell, JJ, Qin, S, Unutmaz, D, Soler, D, Murphy, KE, Hodge, MR *et al.* (2001). Unique subpopulations of CD56+ NK and NK-T peripheral blood lymphocytes identified by chemokine receptor expression repertoire. *J Immunol* **166**: 6477–6482.
20. Mrowietz, U, Schwenk, U, Maune, S, Bartels, J, Küpper, M, Fichtner, I *et al.* (1999). The chemokine RANTES is secreted by human melanoma cells and is associated with enhanced tumour formation in nude mice. *Br J Cancer* **79**: 1025–1031.
21. Burke, F, Relf, M, Negus, R and Balkwill, F (1996). A cytokine profile of normal and malignant ovary. *Cytokine* **8**: 578–585.
22. Niwa, Y, Akamatsu, H, Niwa, H, Sumi, H, Ozaki, Y and Abe, A (2001). Correlation of tissue and plasma RANTES levels with disease course in patients with breast or cervical cancer. *Clin Cancer Res* **7**: 285–289.
23. Luboshits, G, Shina, S, Kaplan, O, Engelberg, S, Nass, D, Lifshitz-Mercer, B *et al.* (1999). Elevated expression of the CC chemokine regulated on activation, normal T cell expressed and secreted (RANTES) in advanced breast carcinoma. *Cancer Res* **59**: 4681–4687.
24. Vaday, GG, Peehl, DM, Kadam, PA and Lawrence, DM (2006). Expression of CCL5 (RANTES) and CCR5 in prostate cancer. *Prostate* **66**: 124–134.
25. Wilcox, RA, Wada, DA, Ziesmer, SC, Elsawa, SF, Comfere, NI, Dietz, AB *et al.* (2009). Monocytes promote tumor cell survival in T-cell lymphoproliferative disorders and are impaired in their ability to differentiate into mature dendritic cells. *Blood* **114**: 2936–2944.
26. König, JE, Senge, T, Allhoff, EP and König, W (2004). Analysis of the inflammatory network in benign prostate hyperplasia and prostate cancer. *Prostate* **58**: 121–129.
27. Murooka, TT, Rahbar, R and Fish, EN (2009). CCL5 promotes proliferation of MCF-7 cells through mTOR-dependent mRNA translation. *Biochem Biophys Res Commun* **387**: 381–386.
28. Kurooka, M and Kaneda, Y (2007). Inactivated Sendai virus particles eradicate tumors by inducing immune responses through blocking regulatory T cells. *Cancer Res* **67**: 227–236.
29. Fujihara, A, Kurooka, M, Miki, T and Kaneda, Y (2008). Intratumoral injection of inactivated Sendai virus particles elicits strong antitumor activity by enhancing local CXCL10 expression and systemic NK cell activation. *Cancer Immunol Immunother* **57**: 73–84.

Published OnlineFirst December 26, 2013; DOI: 10.1158/0008-5472.CAN-13-1283

Molecular and Cellular Pathobiology

Cancer Research

Accumulation of Cytosolic Calcium Induces Necroptotic Cell Death in Human Neuroblastoma

Motonari Nomura[1,2], Ayumi Ueno[1], Kotaro Saga[1], Masahiro Fukuzawa[2], and Yasufumi Kaneda[1]

Abstract

Necrosis has been studied extensively since the early days of medicine, with some patterns of necrosis found to be programmed like apoptotic cell death. However, mechanisms of programmed necrosis (necroptosis) are yet to be fully elucidated. In this study, we investigated how the hemagglutinating virus of Japan-envelope (HVJ-E) induces necrosis in mouse xenografts of human neuroblastoma cells. HVJ-E–induced necrosis in this system was found to depend on phosphorylation of the death receptor kinase receptor interacting protein kinase 1 (RIP1) and on the production of reactive oxygen species. This process was interpreted as necroptosis, based on its suppression by the small molecule necrostatin-1, and it did not involve the TNF-α receptor pathway. We also demonstrated that increased concentrations of cytoplasmic calcium triggered necroptosis by activating calcium-calmodulin kinase (CaMK) II. Finally, we determined that RIP1 phosphorylation was mediated by CaMK II activation. Together, our results define an upstream pathway for the activation of necroptosis in neuroblastoma cells, with potential therapeutic implications. *Cancer Res; 74(4); 1056–66.* ©*2013 AACR.*

Introduction

The way in which a cell dies is decided according to the death stimuli and the endogenous expression level of death signaling effectors. Among the different mechanisms of cell death, there is much more information on apoptosis than necrosis, pyroptosis, or autophagy. Apoptosis is a well-known form of programmed cell death induced by the activation of caspase-8 or -9. Pyroptosis is also a form of caspase-dependent cell death like apoptosis, but the death stimuli are different from apoptosis. In contrast to apoptosis, caspase-1 is activated during the process of pyroptosis by the formation of inflammasome complex, which is induced by the recognition of *Salmonella* and *Shigella* species (1). In addition, a mechanism of cell death was recently identified that is morphologically necrotic but is induced by the same stimuli as apoptosis. This programmed necrotic cell death, which is referred to as necroptosis, is thought to be induced by apoptotic death stimuli, such as TNF-α and Fas ligand. The signal transduction for necroptosis is known to be caspase independent, and its mechanism is as follows: when a ligand binds to the death receptor in the cell, receptor interacting protein kinase 1 (RIP1) is deubiquitinated by CYLD and forms a complex with receptor interacting protein kinase 3 (RIP3), TNF receptor–associated death domain (TRADD), Fas-associated death domain (FADD), and caspase-8. Most human cells express caspase-8, which suppresses RIP1 or RIP3, but if the endogenous expression of caspase-8 is absent, RIP1 remains activated via phosphorylation of serine 161 (2–8). A necrosome consisting of RIP1, RIP3, FADD, and TRADD induces mitochondrial complex I–mediated reactive oxygen species (ROS) production, which is an executor of necroptosis (2, 9). However, the upstream actions of the necroptotic signaling pathway following death receptor stimulation, i.e., the mechanism by which RIP1 is phosphorylated, have not yet been clarified.

Neuroblastoma is one of the most common malignant solid tumors in children and is responsible for 12% of deaths associated with childhood cancer (10). Many genetic features and prognostic factors of neuroblastoma have been revealed. Moreover, most aggressive neuroblastoma cells reportedly do not express caspase-8 (11, 12), a key molecule in the extrinsic pathway of apoptosis. We recently reported a novel strategy for treating aggressive neuroblastoma with UV-treated, nonreplicating Sendai virus [also known as hemagglutinating virus of Japan-envelope (HVJ-E)] particles (13). We also reported that HVJ-E induces necrosis in the xenografts derived from human neuroblastoma cells in severe combined immunodeficient (SCID) mice (13), but the mechanism of this necrotic cell death remains to be solved. Therefore, we reasoned that human neuroblastoma cell lines would be the ideal experimental materials for investigating the mechanism of necroptosis.

In this study, our first objective was to confirm whether the HVJ-E–induced cell death of human neuroblastoma cells is necroptosis, and our second objective was to investigate the

Authors' Affiliations: [1]Division of Gene Therapy Science and [2]Department of Pediatric Surgery, Graduate School of Medicine, Osaka University, Osaka, Japan

Note: Supplementary data for this article are available at Cancer Research Online (http://cancerres.aacrjournals.org/).

Corresponding Author: Yasufumi Kaneda, Division of Gene Therapy Science, Graduate School of Medicine, Osaka University, 2-2 Yamadaoka, Suita, Osaka 565-0871, Japan. Phone: 81-6-6879-3901; Fax: 81-6-6879-3909; E-mail: kaneday@gts.med.osaka-u.ac.jp

doi: 10.1158/0008-5472.CAN-13-1283

Published OnlineFirst December 26, 2013; DOI: 10.1158/0008-5472.CAN-13-1283

mechanism of RIP1 activation during necroptosis in cancer cells.

We concluded that caspase-8–deficient cancer cells, like most neuroblastoma cells, are induced to undergo necroptosis by HVJ-E. The mechanism by which this occurs involves the phosphorylation of RIP1 by calcium-calmodulin kinase (CaMK) II, which is activated by membrane fusion with HVJ-E.

Materials and Methods

Cell lines

The human neuroblastoma cell lines SK-N-SH and SK-N-AS were obtained from the European Collection of Animal Cell Cultures, and the monkey kidney cell line LLCMK2 and human prostate cancer cell line PC3 were from the American Type Culture Collection (ATCC). The SK-N-SH, SK-N-AS, and PC3 cells were maintained in Dulbecco's Modified Eagle Medium (DMEM; Nacalai Tesque Inc.), and the LLCMK2 cells were maintained in Minimum Essential Medium (Gibco-BRL). All media was supplemented with 10% FBS, 100 IU/mL penicillin, and 100 μg/mL streptomycin. The cells were incubated at 37°C in a humidified atmosphere of 95% air and 5% CO_2.

Preparation of HVJ-E

HVJ (VR-105 parainfluenza1 Sendai/52, Z strain from the ATCC) was amplified in the chorioallantoic fluid of 10- to 14-day-old chicken eggs and then purified by centrifugation and inactivated by UV irradiation (99 mJ/cm^2), as previously described (14). The inactivated virus lost its ability to engage in genome replication and protein synthesis but retained its membrane fusion activity (14).

Generation of WT-HVJ-E, ΔHN–HVJ-E, and F_1/F_2-WT-HVJ-E

The majority of the experimental procedures have been previously reported (15). For wild-type (WT)–HVJ-E, the culture medium of HVJ-infected LLCMK2 cells was passed through a filter and then centrifuged at 100,000 × *g* for 2 hours at 4°C to precipitate the WT-HVJ particles. WT-HVJ was inactivated by UV irradiation. For Δ hemagglutinin neuraminidase (HN)–HVJ-E, the WT-HVJ particles were heated at 65°C for 30 minutes, thus denaturing the HN protein. F_1/F_2-WT-HVJ-E was prepared by treating WT-HVJ-E with 5 μg/mL trypsin for 30 minutes at 37°C.

Transmission electron microscopy

Cells were fixed with 2.5% glutaraldehyde in 0.1 mol/L phosphate buffer (pH 7.4) at 4°C and postfixed in 1% OsO_4 solution at 4°C for 1 hour. The samples were then dehydrated in a graded ethanol series and embedded in Quetol 812 epoxy resin (Nissin EM). Ultrathin sections (80 nm) were cut on a Reichert ultramicrotome (Ultracut E; Leica Microsystems), stained with uranyl acetate and lead citrate, and examined with a Hitachi H-7650 electron microscope (Hitachi).

Cell proliferation assay

A MTS assay was performed with the CellTiter 96 AQueous One Solution Cell Proliferation Assay Kit (Promega) to evaluate cell viability. Cells were seeded in 24-well plates (5 × 10^4 cells per well in 500 μL of medium). Twenty-four hours later, the cells were treated with HVJ-E [multiplicity of infection (MOI) of 100–10,000], 0.1 to 10 ng/mL of human recombinant TNF-α (BD Biosciences), or 0.1 to 10 μmol/L of the calcium ionophore A23187 (Sigma-Aldrich Japan, Inc.). Twenty-four hours after this treatment, 100 μL of CellTiter 96 AQueous One Solution Reagent was added to each well, and the plates were incubated at 37°C. After transferring 100 μL of the incubation medium from each well to a new 96-well plate, the absorbance was measured at 490 nm.

Western blotting

Anti–caspase-3, anti–caspase-8, anti–caspase-9, anti-PARP, anti-RIP1, anti-TNFR1, anti–pan-CaMK II, and anti–phospho-CaMK II antibodies were purchased from Cell Signaling Japan Technology K.K., and the anti–β-actin antibody was purchased from Sigma-Aldrich Japan, Inc. The anti-RIP3 antibody was purchased from Santa Cruz Biotechnology, Inc. The anti-HN and -F antibodies were from Scrum Inc. Horseradish peroxidase–conjugated donkey anti-rabbit IgG (GE Healthcare) was used as the secondary antibody for the detection of caspase-3, caspase-9, PARP, RIP1, TNFR1, pan-CaMK II, phospho-CaMK II, HN, and F. Horseradish peroxidase–conjugated sheep anti-mouse IgG (GE Healthcare) was used as the secondary antibody for the detection of caspase-8 and β-actin. Horseradish peroxidase–conjugated chicken anti-goat IgG (R&D Systems) was used as the secondary antibody for the detection of RIP3. Cell lysates were separated using polyacrylamide gels, and the proteins were transferred onto polyvinylidene difluoride membranes. The membranes were then blocked with blocking buffer (TBS containing 0.1% Tween 20 and 3% skim milk) for 1 hour and incubated with primary antibody in blocking buffer at 4°C overnight. The membranes were then washed with washing buffer (TBS containing 0.1% Tween 20) and incubated with the horseradish peroxidase–conjugated anti-mouse, anti-goat, or anti-rabbit secondary antibody (GE Healthcare) in blocking buffer for 1 hour. Signals were detected with Chemi-Lumi One (Nakalai Tesque Inc.) according to the manufacturer's instructions.

Measurement of ROS production

ROS generation was detected using a fluorescence probe called MitoSOX, which detects mitochondrial superoxide production. The cells were pretreated with 5 μmol/L MitoSOX at 37°C for 10 minutes according to the manufacturer's instructions.

Estimation of the intracellular Ca^{2+} concentration

The intracellular Ca^{2+} concentration was estimated with the Fura 2 Kit (DOJINDO) according to the manufacturer's protocol. Briefly, SK-N-SH cells (1 × 10^4 cells) were seeded in a 96-well plate and incubated overnight. Then, the medium was removed, and the manufacturer's loading buffer was added to the cells. The cells were incubated at 37°C for 1 hour, and the buffer was replaced with recording buffer containing Fura 2-acetoxymethyl ester. Next, 1,000 MOI of HVJ-E with WT HN–inactivated F (WT.HN-F0) or WT HN-activated

Published OnlineFirst December 26, 2013; DOI: 10.1158/0008-5472.CAN-13-1283

F (WT.HN-F1/F2) were added to each well, and the resulting fluorescence intensity was estimated by recording the absorbance at the peak excitation wavelength of 340/380 nm and the peak emission wavelength of 510 nm.

Detection of apoptosis and necrosis

Following treatment with HVJ-E or A23187, SK-N-SH cells or the removed xenografts were fixed with 4% paraformaldehyde, and apoptosis or necrosis was detected with the GFP-Certified Apoptosis/Necrosis Detection System Kit (Enzo Life Science Inc.) according to the manufacturer's protocol.

Pretreatment of cells with inhibitors

To inhibit the activity of pan-caspase, 20 μmol/L Z-VAD-FMK (Medical & Biological Laboratories) was added to the cells 1 hour before treatment with HVJ-E. To inhibit the activity of RIP1, 20 μmol/L necrostatin-1 (Enzo Life Science Inc.) was added to the cells 24 hours before exposure to HVJ-E. To inhibit the increase of cytoplasmic Ca^{2+}, 10 μmol/L BAPTA-AM (Sigma-Aldrich Japan, Inc.) was added to the cells 30 minutes before exposure to HVJ-E or A23187. To inhibit the activity of CaMK II, 20 μmol/L CK59 (EMD Millipore) was added to the cells 1 hour before HVJ-E exposure.

Cell transfection with siRNA

SiGENOME SMARTpool Human RIP1 (M-004445-02-0005; Thermo Fisher Scientific), siGENOME SMARTpool Human RIP3 (M-003534-01-0005; Thermo Fisher Scientific), or ON-TARGET plus Human CAMK IIα siRNA SMARTpool (L-004942-00-0005; Thermo Fisher Scientific) was used to transfect SK-N-SH cells. The siGENOME Non-Targeting siRNA Pool (D-001206-13-05; Thermo Fisher Scientific) was used as a control. The siRNA transfection was performed as follows: siRNA and Lipofectamine RNAiMAX (Invitrogen) were mixed in Opti-MEM and incubated for 20 minutes at room temperature, and then the mixture was added to cultured SK-N-SH cells in 6- or 24-well plates. The cells were incubated for 4 hours at 37°C, and the medium was exchanged with DMEM. The siRNA dosage was 100 or 20 pmol/well. The knockdown efficiency was confirmed by Western blotting at 72 hours after transfection.

Labeling of cancer cells with ^{32}P-orthophosphate and immunoprecipitation

SK-N-SH cells [1×10^6 cells per immunoprecipitation (IP) sample] were seeded 1 day before the labeling experiment, resuspended in phosphate-free medium, and incubated for 40 minutes at 37°C. The cells were centrifuged and resuspended in phosphate-free medium containing 0.1 mCi of ^{32}P-orthophosphate (Perkin Elmer, Inc.) and incubated for 2 hours before stimulation with 1,000 MOI of HVJ-E for 2 hours. In some experiments, 20 μmol/L necrostatin-1 or 20 μmol/L CK-59 was added to the cells before HVJ-E stimulation. The cells were treated with HVJ-E for 2 hours before cell lysis. For immunoprecipitation, the cell lysates were precleared using 5 μg of the Normal Rabbit IgG–Agarose Conjugate (Santa Cruz Biotechnology, Inc.) plus 30 μL of Protein A Agarose Fast Flow (Millipore) for 1 hour at 4°C. The agarose beads and nonspecifically associating proteins were removed by centrifugation at 12,000 × *g* for 10 minutes at 4°C. The supernatant was incubated with 5 μg of anti-RIP1 antibody or Rabbit Control IgG (ChiP grade; Abcam) plus 30 μL of Protein A Agarose Fast Flow for 12 hours at 4°C. The agarose beads were centrifuged at 3,000 × *g* for 2 minutes at 4°C, washed three times, and centrifuged as described above. The washed beads were boiled three times for 5 minutes at 95°C and resolved by SDS–PAGE. The gel was dried and subjected to autoradiography.

Statistical analyses

The data are expressed as the means ± SD. A two-tailed unpaired Student *t* test was used to determine the statistical significance of the difference between two groups. Probability values of $P < 0.05$ were considered to be statistically significant.

Results

HVJ-E induces necrotic cell death in neuroblastoma cells

We first analyzed the morphologic changes induced by HVJ-E in SK-N-SH cells. Twenty-four hours after the treatment of SK-N-SH cells with 1,000 MOI of HVJ-E, we observed swollen nuclei by transmission electron microscopy (Fig. 1A). Whether the whole cell body was swollen by HVJ-E could not be confirmed because the cells were fused together (Supplementary Fig. S1A). A MTS assay showed that the cell viability significantly decreased in a dose-dependent manner following treatment with different MOIs (100, 1,000, or 10,000) of HVJ-E in SK-N-SH and SK-N-AS cells (Fig. 1B). The HVJ-E–induced cell death was not significantly suppressed by the pretreatment with cytochalasin D, which binds to actin filaments and thus blocks actin polymerization, suggesting that cell fusion does not contribute to this cell death (Supplementary Fig. S1B).

HVJ-E–induced cell death in neuroblastoma cells is not apoptosis but necroptosis

Although we observed morphologic changes in necrotic SK-N-SH cells, we next needed to analyze the degree at which apoptosis contributes to this cell death. The cleavage of caspase-9, caspase-3, and PARP was detected by Western blot analysis at 12 hours after treatment with 1,000 MOI of HVJ-E, but caspase-8 was not endogenously expressed (Fig. 2A). However, the inhibition of PARP cleavage by Z-VAD-FMK could not significantly suppress HVJ-E–induced cell death (Fig. 2B and C). These results imply that this cell death is not caspase-dependent apoptosis. We could not narrow down the key factors responsible for HVJ-E–induced cell death. Therefore, we exhaustively investigated the changes in gene expression during this process by microarray analysis. However, no remarkable changes in the expression of individual genes were detected. Hence, we subjected the expressed genes to pathway analysis using MetaCore v6.5. The pathway analysis showed significant changes in some

Published OnlineFirst December 26, 2013; DOI: 10.1158/0008-5472.CAN-13-1283

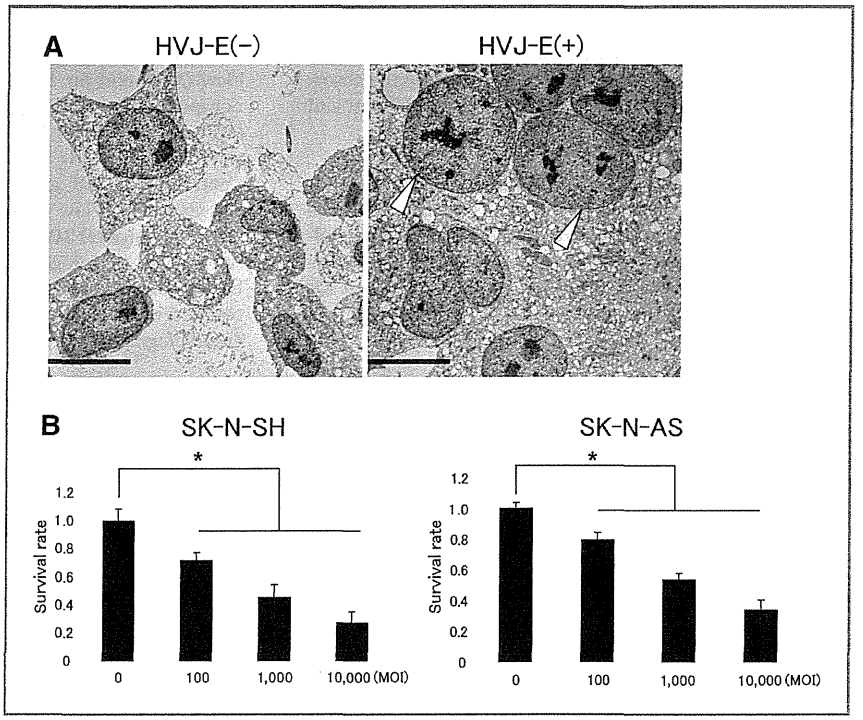

Figure 1. Neuroblastoma cell death induced by HVJ-E. A, 24 hours after the treatment of SK-N-SH cells with 1,000 MOI of HVJ-E, the swollen nuclei (arrowhead) of the cells were observed by electron microscopy. Scale bar, 10 μm. B, the treatment of SK-N-SH and SK-N-AS cells (3×10^5 cells) with HVJ-E for 24 hours resulted in the cell death in a dose-dependent manner. Each survival value (mean ± SD; $n = 4$) was the ratio of the value with treatment to the value without treatment. *, $P < 0.05$.

pathways, including oxidative phosphorylation, ubiquinone metabolism, cytoskeleton remodeling, the immune response, and others (data not shown). Of these processes, we focused on the oxidative phosphorylation pathway because it produces ROS, which is one of the key executors of necrosis. Taking into consideration our findings on the

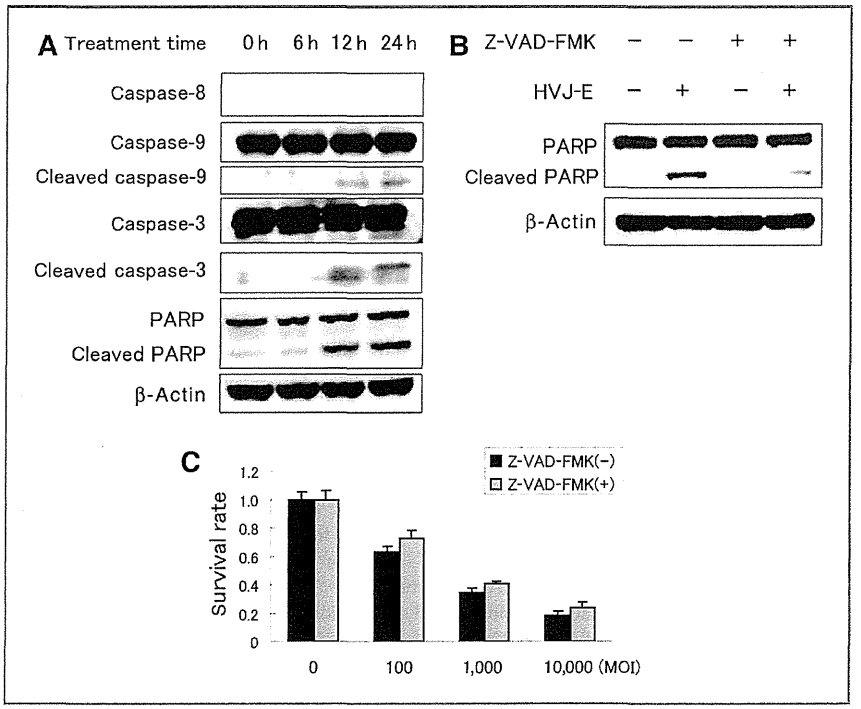

Figure 2. HVJ-E–induced cell death in SK-N-SH cells is not caspase-dependent apoptosis. A, SK-N-SH cells (3×10^5 cells) were treated with 1,000 MOI of HVJ-E for 6, 12, or 24 hours. The cleavage of caspase-9, caspase-3, and PARP was observed 12 hours after HVJ-E exposure, but caspase-8 was not endogenously expressed. B, the HVJ-E–induced cleavage of PARP was inhibited by pretreatment with Z-VAD-FMK. C, the HVJ-E–induced cell death was not significantly suppressed by pretreatment with Z-VAD-FMK. The experiments were performed in triplicate, and representative results are shown. Each survival value (mean ± SD; $n = 4$) was the ratio of the value with treatment to the value without treatment.